© 2023. Published by The Company of Biologists Ltd | Journal of Cell Science (2023) 136, jcs260753. doi:10.1242/jcs.260753

TOOLS AND RESOURCES

Confinement plus myosin-II suppression maximizes heritable loss of chromosomes, as revealed by live-cell ChReporters

Brandon H. Hayes[1,*], Peter Kuangzheng Zhu[1,*], Mai Wang[1,*], Charlotte R. Pfeifer[1], Yuntao Xia[1], Steven Phan[1], Jason C. Andrechak[1], Junhong Du[1], Michael P. Tobin[1], Alisya Anlas[1], Lawrence J. Dooling[1], Manasvita Vashisth[1], Jerome Irianto[1], Michael A. Lampson[2] and Dennis E. Discher[1,‡]

ABSTRACT

The mechanical environment of a cell can have many effects, but whether it impacts the DNA sequence of a cell has remained unexamined. To investigate this, we developed a live-cell method to measure changes in chromosome numbers. We edited constitutive genes with GFP or RFP tags on single alleles and discovered that cells that lose Chromosome reporters (ChReporters) become non-fluorescent. We applied our new tools to confined mitosis and to inhibition of the putative tumor suppressor myosin-II. We quantified compression of mitotic chromatin *in vivo* and demonstrated that similar compression *in vitro* resulted in cell death, but also rare and heritable ChReptorter loss. Myosin-II suppression rescued lethal multipolar divisions and maximized ChReporter loss during three-dimensional (3D) compression and two-dimensional (2D) lateral confinement, but not in standard 2D culture. ChReporter loss was associated with chromosome mis-segregation, rather than just the number of divisions, and loss *in vitro* and in mice was selected against in subsequent 2D cultures. Inhibition of the spindle assembly checkpoint (SAC) caused ChReporter loss in 2D culture, as expected, but not during 3D compression, suggesting a SAC perturbation. Thus, ChReporters enable diverse studies of viable genetic changes, and show that confinement and myosin-II affect DNA sequence and mechano-evolution.

KEY WORDS: Confinement, Compression, Myosin, Rigidity, Aneuploidy, Heritability

INTRODUCTION

For cells in interphase, the expression of genes, as well as the structure and function of cells, is regulated by their mechanical microenvironment, such as tissue stiffness, two-dimensional (2D) or three-dimensional (3D) confinement, and even modest stretching (Engler et al., 2006; Meng et al., 2018; Nava et al., 2020; Paszek et al., 2014; Petridou et al., 2021; Przybyla et al., 2016; Segel et al., 2019; Uhler and Shivashankar, 2017). Myosin-II is often a key factor (Parajon et al., 2021), but myosin-II also has roles in cell division, such as mitotic rounding of animal cells, which counteracts 3D compression (Fig. 1A) (Sedzinski et al., 2011; Stewart et al., 2011). Intriguingly, in rigid yeast, deletion of myosin-II somehow leads to heritable chromosome losses and gains (Rancati et al., 2008). Furthermore, knockdown of non-muscle myosin-IIA in the dense and stiff 3D tissue of mouse embryo skin reproducibly causes cancer (Conti et al., 2015; Schramek et al., 2014). Given that genetic changes typically drive cancer and are far more numerous in tumors that arise in solid tissues (Davoli et al., 2013; Tomasetti and Vogelstein, 2015; Pfeifer et al., 2017), we hypothesized that suppressing myosin-II could directly increase viable genetic changes – particularly when cell division is confined.

Errors are possible with every mitosis, and some perturbations can increase the likelihood of viable errors. However, it remains a grand challenge to predict whether any abnormal mitotic event will lead to cell death, arrest or heritable genetic changes that add DNA diversity for subsequent selection. Mitotic compression distorts the microtubule (MT) spindle and causes acute mis-segregation of chromosomes, but it also kills some cells quickly via 'lethal multipolar divisions' and other pathways (Dumont and Mitchison, 2009; Lancaster et al., 2013; Matthews et al., 2020). The heritable losses or gains of chromosomes (i.e. aneuploidy) resulting from mechanical processes are thus not trivial and have remained unexamined.

Constraints imposed by 2D micropatterns have revealed that inhibiting myosin-II with blebbistatin can disrupt centriole separation, leading to speculation that this key mechanobiology motor might act in fundamental mechanisms of aneuploidy prevention (Vitiello et al., 2019). Although initial studies using blebbistatin in standard 2D cultures suggested that inhibition of cleavage furrow contraction did not disrupt mitosis (Straight et al., 2003), subsequent studies with this reversible inhibitor and with knockdowns have concluded that division is perturbed (Ma et al., 2010; Rosenblatt et al., 2004; Taneja et al., 2020). However, only one recent study of 2D cultures claimed increased frequency of abnormal chromosome segregation upon blebbistatin treatment and speculated that this is correlated with aneuploidy (Booth et al., 2019). Any roles for myosin-II in heritable aneuploidy – whether in 2D or 3D microenvironments – remain speculative but could be important to oncogenesis.

To visualize the loss (and potentially gain) of a chromosome and track viability, we use gene editing to create a 'ChReporter' by fusing GFP or RFP (hereafter GFP/RFP) to a candidate 'constitutive' gene on one allele of a chosen chromosome (i.e. Chr-5, -9, -12 and/or -19) (Fig. 1A). Loss of the GFP/RFP signal allows us to then identify individual cells and colonies before, during and after the change – with chromosome loss for some tagged genes made clear by end-stage genetic analyses. This approach provides definitive evidence of viability and heritability, unlike inferences from sequencing of extracted DNA and RNA, which is error prone (Yizhak et al., 2019) and limited in the detection of rare cells (<1%). High sensitivity is crucial to

[1]Mol. Cell Biophysics Lab, University of Pennsylvania, Philadelphia, PA 19104, USA. [2]Department of Biology, University of Pennsylvania, Philadelphia, PA 19104, USA.
*These authors contributed equally to this work

‡Author for correspondence (discher@seas.upenn.edu)

B.H.H., 0000-0002-9099-201X; J.C.A., 0000-0002-6659-9488; M.V., 0000-0002-2280-5980; J.I., 0000-0002-4804-7225; M.A.L., 0000-0002-2825-1894; D.E.D., 0000-0001-6163-2229

Handling Editor: Andrew Ewald
Received 25 October 2022; Accepted 27 April 2023

Journal of Cell Science (2023) 136, jcs260753. doi:10.1242/jcs.260753

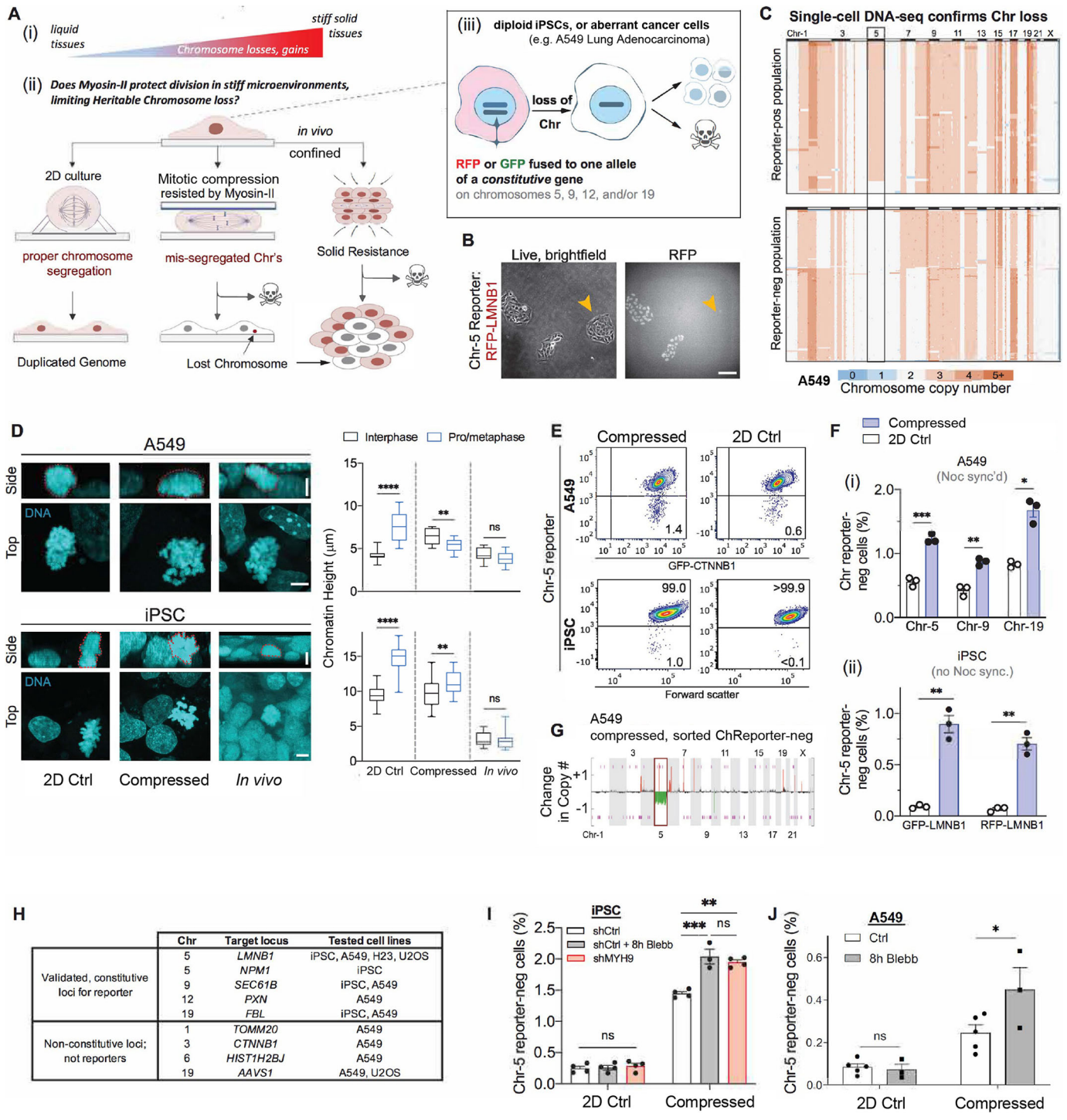

	Chr	Target locus	Tested cell lines
Validated, constitutive loci for reporter	5	*LMNB1*	iPSC, A549, H23, U2OS
	5	*NPM1*	iPSC
	9	*SEC61B*	iPSC, A549
	12	*PXN*	A549
	19	*FBL*	iPSC, A549
Non-constitutive loci; not reporters	1	*TOMM20*	A549
	3	*CTNNB1*	A549
	6	*HIST1H2BJ*	A549
	19	*AAVS1*	A549, U2OS

Fig. 1. See next page for legend.

understanding initial changes that eventually give rise to new populations through selection.

For our confinement-induced ChReporter loss studies, we focus on mitotic confinement, whereas interphase cells are not confined in most of our studies. Cells studied are: (1) solid tumor-derived lines (e.g. A549 lung adenocarcinomas) and (2) genomically stable induced pluripotent stem cells (iPSCs), which serve as a model for both normal tissue and tumor stem cells (Mandai et al., 2017; Skamagki et al., 2017). Heritable changes in the DNA of a cell ultimately prove to be a consequence of confining microenvironments that drive mechano-evolution.

RESULTS

Myosin-II mechanoprotects against chromosome loss in confined mitosis

Within days of using flow cytometry to sort A549, iPSCs or another cell line with a GFP/RFP-tagged allele, we observe in standard 2D cultures the loss of GFP/RFP in very rare cell colonies (~0.1%) (Fig. 1B; Fig. S1A–D). Note that we choose a presumed constitutive gene that also localizes to a specific organelle, such as the nucleus with RFP–LMNB1, which helps to minimize uncertainty caused by autofluorescence or other stains. The GFP/RFP-negative colonies

Journal of Cell Science (2023) 136, jcs260753. doi:10.1242/jcs.260753

Fig. 1. Live-cell tracking of monoallelic RFP **or** GFP fusions to constitutive alleles shows mitotic compression drives chromosome loss. (A) Chromosome (Chr) losses and other genetic changes are highest in tissues that are both stiff and proliferative (i), motivating development of a live-cell chromosome reporter (ChReporter). (ii) Mitotic perturbations potentially affect chromosome loss and/or viability; maximal rounding in 2D culture is suppressed when cells are compressed *in vitro* or surrounded *in vivo* by cells and matrix. (iii) Alleles are identified that are constitutively expressed even when fused to GFP or RFP. (B) Colonies of RFP-positive and (arrowhead) RFP-negative A549 cells engineered with a Chr-5 reporter in which one *LMNB1* allele has an N-terminal RFP sequence. Cells were flow-sorted and plated sparsely for ∼1 week. Scale bar: 100 µm. (C) Single-cell DNA sequencing reveals both expected and unexpected chromosome (Chr) losses and gains in A549 cells with the RFP–LMNB1 reporter, after isolation via FACS. Each row shows the whole genome at 1.5 Mb resolution for one of 61 RFP-positive or 140 RFP-negative cells. Note A549 cells typically have three copies of Chr-5. (D) Images of chromatin and plots of chromatin height in iPSCs and A549 cells in standard 2D culture or that were under compression, or from 3D *in vivo* teratomas or tumors engrafted at subcutaneous sites in immunodeficient mice ($n \geq 30$ cells per condition; the box represents the 25–75th percentiles, and the median is indicated; the whiskers show the 5–95% range). **$P<0.005$; ****$P<0.0001$; ns, not significant (Mann–Whitney *U*-rank test). Scale bars: 5 µm. (E) Flow cytometry analyses of Chr-5 reporter loss in iPSCs and A549 cells in either compression or 2D cultures. Numbers are the percentage of cells in highlighted sector. (F) Flow cytometry results: (i) Noc-synchronized A549 cells with three different reporters, or (ii) two distinct iPSC clones with no synchronization (∼10 h doubling of iPSCs is ∼3 times faster than A549 cells) ($n=3$ replicates, mean±s.e.m.). *$P<0.05$, **$P<0.005$, ***$P<0.0005$ (unpaired two-tailed *t*-test with Welch's correction). (G) Flow sorted cells isolated immediately after compression validates ChReporter loss in A549 cells, through SNPa analyses. (H) Designs for various loci and cell lines, with some proving to be constitutively expressed and validated as bona fide ChReporters. The lower half of table indicates loss of some loci that do not correspond to chromosome loss. (I,J) Flow cytometry results for ChReporter-negative iPSCs (I) and imaging results for A549 cells (J). Both show increases under rigid compression with myosin-IIA suppression (knockdown or inhibition with 20 µM blebbistatin) but no effects in standard 2D culture ($n=3$ or 4; mean±s.e.m.). *$P<0.05$, **$P<0.005$; ***$P<0.0005$; ns, not significant (three-way ANOVA with Tukey's correction for multiple comparisons).

demonstrate viability and heritability, and detachment followed by flow cytometry sorting enables us to investigate the molecular basis of GFP/RFP loss using a range of methods, such as single-cell sequencing, bulk array technologies, and low-throughput metaphase spreads, among other approaches (Fig. 1C; Fig. S1E–I). It is currently challenging or impossible for genetic methods to confidently detect loss of a particular gene in just 1% of cells within a bulk population, especially if spatial information, such as colony formation, is needed to prove the viability and heritability that is essential to the biology (i.e. the study of life, not death). Fluorescence-based sorting of A549 cells subjected to single-cell sequencing here not only showed the hoped-for chromosome loss, and hence the validation of a bona fide ChReporter, but also revealed losses and gains of other chromosomes in rare cells. This evidence of spontaneous, but very low levels of, genetic instability in A549 cells in 2D culture contrasted with the relative lack (<0.1%) of ChReporter-negative iPSCs from standard 2D cultures, which single-cell sequencing also showed (Fig. S1C).

Before studying the possible effects on ChReporter loss with mitotic compression, we first addressed whether mitotic compression occurs *in vivo* and if so, then how much compression occurs. Mitotic and interphase chromatin dimensions were thus analyzed in confocal volumes of human-in-mouse tumors and teratomas. Unlike what was seen in standard 2D cultures where mitotic chromatin rounds up to be taller than interphase chromatin (in side-view, along the *Z*-axis), mitotic and interphase chromatin showed the same heights for both iPSC-derived teratomas and A549 tumors (Fig. 1D). In other words, mitotic chromatin within these solid tissues does not show the rounding up that is typical in 2D culture. Teratomas have a palpably similar rigidity to the tumors that are collagen-rich and stiff (i.e. ∼5 kPa) (Swift et al., 2013), and such a stiffness is within the range of tissues and tumors that associate with high genetic change (Pfeifer et al., 2017, 2018). Compression of mitotic cells in culture was therefore used to suppress the typical mitotic rounding in 2D cultures and thereby mimic the mitotic flattening measured in stiff tissue. Our simple method uses a single ring-weight placed on top of an upper glass coverslip with compression limits provided by rigid polystyrene microbeads mixed with the cells (Fig. S2A). This gives ∼20–30% compression of the mitotic state with no significant effect on interphase heights (Fig. 1D). As noted elsewhere, several experiments were also performed with higher or lower weights (i.e. 2× or 0.7× of the single weight) in order to modulate the mitotic compression. Compressive stress even for ∼8 h sufficed to visibly increase abnormal mitosis, with splayed out chromosomes and suppressed growth but also cell death (Fig. 1D; Fig. S2B–D).

The proportion of viable RFP/GFP-negative cells (i.e. cells that had lost their ChReporters) was quantified by flow cytometry after 16–48 h of recovery in 2D culture post-compression. Loss of various ChReporters was found to be ∼1% for A549 cells and iPSCs, which is ∼2–10 fold higher than in 2D controls (Fig. 1E,F). Flow sorting of RFP-negative A549 cells engineered with a Chr-5 ChReporter was followed by various genetic analyses that showed the expected chromosome loss relative to RFP-positive controls (Fig. 1G). Loss of diverse ChReporters was similarly validated for multiple cell types, including iPSCs (Fig. S1C). However, the approach is non-trivial, with some tagged genes yielding GFP/RFP-negative cells that do not represent a genetic change (Fig. 1H; Fig. S1). Such genes surprisingly include an H2B histone, for example.

To determine whether myosin-II might protect against ChReporter loss and thereby exhibit a tumor suppressor relevant function, the main non-muscle myosin-II isoform myosin-IIA (*MYH9*) was knocked down using shRNA (sh*Myh9*). This was done first in the rapidly dividing iPSCs harboring the Chr-5 ChReporter RFP–LMNB1 (Fig. S2A). Compression of the knockdown cells showed 30–40% more ChReporter loss than compression of controls, whereas cells in 2D culture showed no effect from the knockdown (Fig. 1I). To rule out adaptation to knockdown and to inhibit other myosin-II isoforms, we added the pan-myosin-II inhibitor blebbistatin during the 8 h compression of control cells; such a brief treatment affects the levels of very few proteins compared to knockdown (Raab et al., 2012). Blebbistatin treatment nonetheless showed the same quantitative effect as *MYH9* knockdown – no effect in 2D culture and a significant increase of ChReporter loss under 3D compression. A549 cells gave the same result (Fig. 1J).

The requirement for compression indicates that myosin-II mechanoprotects the integrity of the genome, and the results here provide the first evidence of increased genetic change in myosin-II-suppressed human cells. The results can help explain how *Myh9* knockdown with shRNA in embryonic mouse skin often leads to carcinoma (Schramek et al., 2014). Moreover, skin is a relatively stiff and confining 3D microenvironment (Pfeifer et al., 2017, 2018), which suggests that such confinement is a key unappreciated factor, given that we see genetic effects of myosin-II inhibition *in vitro* only with confinement.

Confinement-induced mis-segregation with myosin-II inhibition shows fewer multipolars

Past studies (Dumont and Mitchison, 2009; Lancaster et al., 2013) have shown that there is a compression-induced inhibition of

Journal of Cell Science (2023) 136, jcs260753. doi:10.1242/jcs.260753

progression to anaphase, and we confirmed such inhibition (Fig. 2A). We discovered that blebbistatin had no effect on this compression-induced suppression of anaphase counts (Fig. 2A). It has been previously shown, via tubulin staining, that there is a significant compression-induced lengthening of mitotic spindles (Dumont and Mitchison, 2009; Lancaster et al., 2013), and we observed that blebbistatin did not affect such lengthening (data not shown). Interphase cells are also well known to have a more dendritic shape with blebbistatin, which we observed, but the drug had no effect on the shape or overall F-actin signal from Rhodamine–phalloidin in mitotic cells (data not shown). A difference between the role of myosin-II and actin in abnormal mitosis has been suggested from previous studies in which addition of the F-actin-depolymerizing drug latrunculin during compression of HeLa cells strongly increases the level of 'lethal multipolar divisions' and also immediate cell death (Lancaster et al., 2013). Consistent with such studies, we also found that multipolar divisions are a significant fraction of the total abnormal mitotic cells in compression, with chromosome bridging-type mis-segregation events accounting for the remaining fraction. We observed no effect of blebbistatin in 2D culture on the latter bridging chromosome events (Fig. 2B,C), which disagrees with one study that reported blebbistatin increases chromosome mis-segregation in 2D culture (Booth et al., 2019); however, under compression, we observed blebbistatin treatment rescued a large fraction of the multipolar divisions (Fig. 2D). Our results are consistent with what has been seen upon inhibition by blebbistatin of centriole separation in pattern-confined cells (Vitiello et al., 2019). The overall percentage of abnormal anaphase cells was not affected by blebbistatin (Fig. 2C), and so blebbistatin treatment in

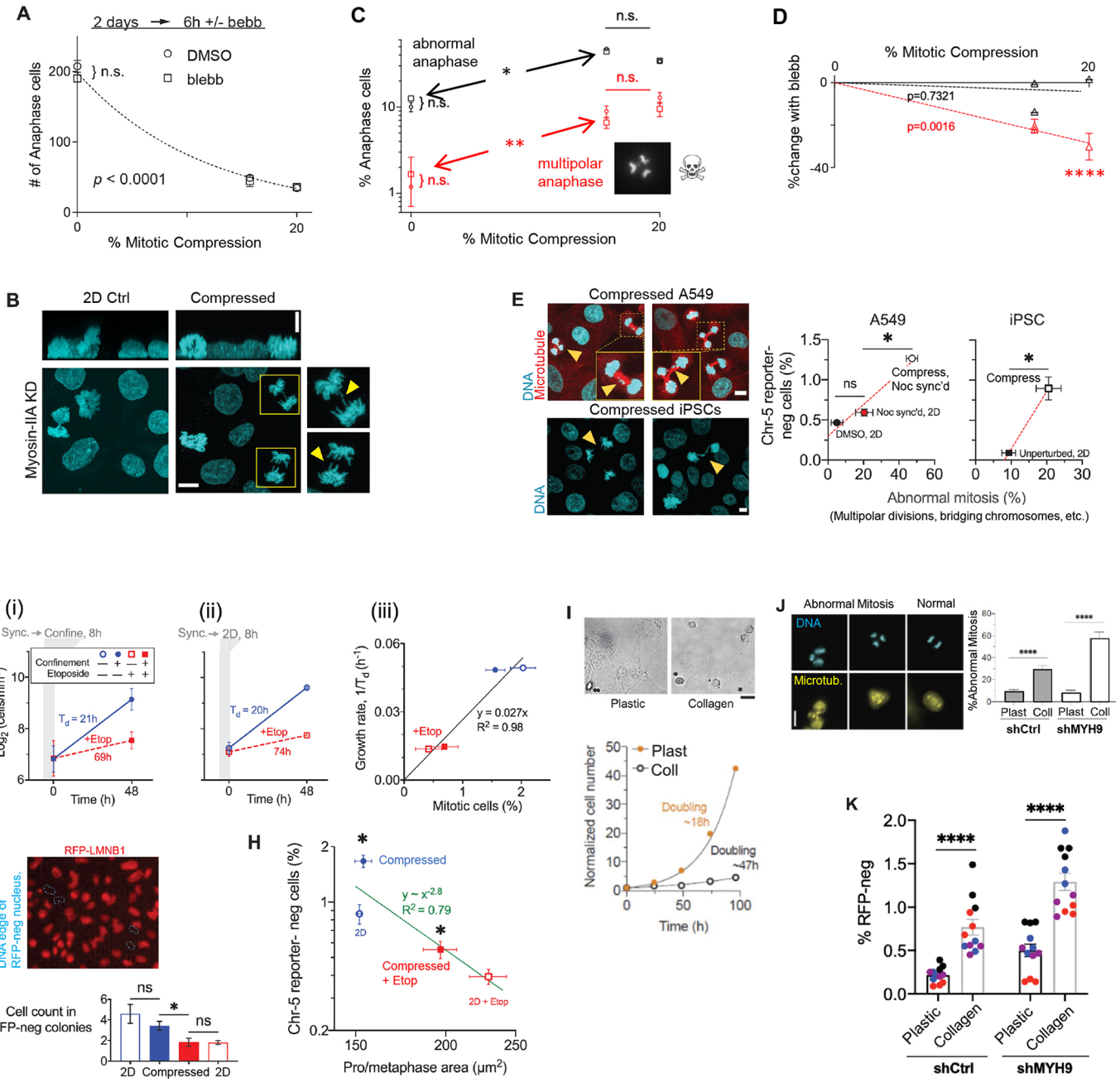

Fig. 2. See next page for legend.

Journal of Cell Science (2023) 136, jcs260753. doi:10.1242/jcs.260753

Fig. 2. Mitosis of compressed cells combined with myosin-II inhibition increases viable chromosome mis-segregation and ChReporter loss. (A) A549 cells plated for 2 days were compressed ∼20% as per Fig. 1D–J or slightly less for 6 h with or without blebbistatin treatment (as per Fig. 1J). Cells were then fixed, stained and imaged for anaphase counts. Blebbistatin has no effect (unpaired two-tailed *t*-test; n.s., not significant). Curve is shown as a guide for the eye. (*n*=3–6 replicates; mean±s.e.m.). *P*<0.0001 (log-linear model for non-zero slope). (B) iPSCs with knockdown of non-muscle myosin-IIA (MYH9) have abnormal mitoses when under compression (yellow arrowheads, bridging chromosomes), whereas control knockdown cells only show normal mitoses, indicating shMYH9 does not affect basal instability. Scale bars: 10 µm. (C) The proportion of cells with an abnormal anaphase increases with compression but is independent of blebbistatin (black trace, key as in A). The proportion of anaphase cells with multipolar events also increases with compression (red trace) (*n*=3–6 replicates, mean±s.e.m.). **P*<0.05, ***P*<0.005 (unpaired two-tailed *t*-test with Welch's correction). (D) Compression-induced multipolar events are suppressed by blebbistatin. Black, abnormal anaphases; red, multipolar events (*n*=3–6 replicates, mean ±s.e.m.). *P*=0.0016 for non-zero slope; *****P*<0.0001 (unpaired two-tailed *t*-test with Welch's correction). (E) Images of abnormal mitosis and flow cytometry measures of the percentage of Chr-5 reporter-negative cells plotted against percentage of abnormal mitosis for A549 cells and iPSCs. Yellow arrowheads, bridging chromosomes or cells undergoing multipolar division (*n*=3 replicates, mean±s.e.m.). **P*<0.05 (unpaired two-tailed *t*-test with Welch's correction). Scale bars: 5 µm. (F) TOP2A inhibition with etoposide (1 µM) during compression (time indicated with gray shading in i and ii) of Noc-synchronized A549 cells. Proliferation remains suppressed even after drug washout. (iii) Mitotic count measurements are proportional to growth rates (*n*=3, mean±s.e.m.). (G) Image of RFP–LMNB1 showing the most nuclei have signal, but blue outlines indicate DNA outlines of rare RFP-negative cells nuclei, which form colonies. Graph shows cell numbers per colony forming unit (CFU) of ChReporter-negative cells, which Etop suppresses (*n*=3 replicates, mean±s.e.m.). **P*<0.05; ns, not significant (two-way ANOVA with Tukey's correction for multiple comparisons). (H) ChReporter loss decreases with Etop, correlating with pro-metaphase area (*n*=3 replicates, mean±s.e.m.) **P*<0.05 (two-way ANOVA with Tukey's correction for multiple comparisons). (I) A549 cells spread on plastic but are always round and laterally confined, whereas they attach firmly on dense collagen-coated soft gel, which suppresses proliferation by ∼2–3-fold. Plot of growth is representative (*n*=4 experiments). Scale bar: 50 µm. (J) Abnormal mitosis is more frequent on collagen-coated gels versus plastic, in both myosin-IIA-depleted cells and shCtrl cells (*n*≥10 cells per condition; mean ±s.e.m.). *****P*<0.0001 (unpaired two-tailed *t*-test with Welch's correction). Scale bar: 20 µm. (K) ChReporter RFP-negative cells occur more frequently on collagen-coated gels versus plastic (*n*=4 triplicates, in four colors; mean ±s.e.m.). ***P*<0.005; ****P*<0.0005 (three-way ANOVA with Tukey's correction for multiple comparisons).

compressed cells increases the fraction of more-tolerated bridging events, while decreasing the fraction of lethal multipolar divisions. Such a shift toward survivable mis-segregation events thus explains increased ChReporter loss with myosin-II inhibition in mitotic compression (Fig. 1J).

Mitotic chromatin is flattened and compacted by compression (Fig. 2B; Fig. S2A), whereas interphase cells are shorter and are minimally affected (Fig.1D). The fraction of ChReporter-negative cells was generally associated with the visible levels of abnormal mitosis (Fig. 2E), although abnormal mitosis did not strictly predict chromosome loss; some iPSCs indeed showed abnormal mitosis but no ChReporter loss, whereas A549 cells showed the opposite. The proportion of cells showing ChReporter loss was far below the fraction of cells exhibiting abnormal mitosis (∼15-fold for iPSCs, and ∼60-fold for A549 cells), which seems consistent with losses of untagged chromosomes, as well as Chr-9 and Chr-19 ChReporter results (Fig. 1F). Some studies have used transient nocodazole (Noc) to synchronize A549 cell division before compression, and when we treat cells with Noc a residual effect of this (after drug washout) fits the overall trend for A549 cells of ChReporter-negative cells versus abnormal mitosis events (Fig. 2E, left plot). This agrees with known effects of Noc-induced disassembly of spindle MTs (Thompson and Compton, 2008).

To assess the effect of cell division on ChReporter loss, the topoisomerase-IIα inhibitor etoposide (Etop) was added at a low non-toxic dose (Nielsen et al., 2020) during the 8 h compression. Etop suppressed subsequent growth and mitotic counts (Fig. 2F) as well as the proportion of ChReporter-negative cells and their colony size, which indicates that loss of the tagged chromosome is a heritable change to the DNA of a living cell rather than a senescence-inducing or lethal event (Fig. 2G,H). Viable A549 cells re-spread their decondensed chromatin in interphase, re-assemble their lamina and proliferate to generate ChReporter-negative colonies (Fig. 2G, bar graph). In 2D cultures, TOP2A drives compaction of mitotic chromatin (Farr et al., 2014; Samejima et al., 2012), which Etop inhibited (Fig. 2H). Importantly, compressed mitosis combined with Etop treatment modestly rescued the compaction defect and also slightly increased ChReporter loss (Fig. 2H). Results from these Etop experiments suggest that the total number of cell divisions (*N*) is a key determinant of chromosome loss.

2D substrates with a dense collagen-coating can limit cell spreading – especially for soft substrates (Engler et al., 2004). We postulated that this could allow us to test the effects of lateral confinement on ChReporter loss, especially given that previous results from 2D micropattern constraints suggest that myosin-II might have a fundamental role in aneuploidy prevention (Vitiello et al., 2019). We found that A549 proliferation was suppressed on collagen-coated substrates (Fig. 2I), and abnormal mitosis was higher (Fig. 2J) as was ChReporter loss (Fig. 2K). These results not only align with those seen upon compression (Fig. 2A–C) but show that myosin-IIA suppression tends to increase abnormal mitosis and ChReporter loss, consistent with the speculated role in aneuploidy (Vitiello et al., 2019). Abnormal mitoses induced by confining microenvironments thus associate better with chromosome loss than does the simple total numbers of divisions (*N*). In other words, the quality of divisions is a factor beyond the mere quantity of divisions. Solid tissues, such as skin are also rich in collagen, which makes them stiff (Swift et al., 2013) and which leads to a prediction that myosin-II suppression will increase ChReporter loss within stiff and constraining solid tissues *in vivo*.

In vivo chromosome loss increases with rigidity-associated divisions and myosin-II suppression

To directly assess the 3D *in vivo* responses of ChReporters, subcutaneous xenografts were made in stiff collagen-rich dermis (Swift et al., 2013). Immunodeficient mice were injected with human iPSCs or A549 cells expressing *LMNB1* Chr-5 ChReporters in order to generate iPSC teratomas or A549 tumors (Fig. 3A; Fig. S2E), and then harvested after ∼2–3 months to flow-sort for rare fluorescence-negative cells and confirm loss of Chr-5 (Fig. 3B). The latter evidence of genetic change argues against there only being mere epigenetic changes in these teratomas and tumors (Shaffer et al., 2017). Analysis of disaggregated teratomas and tumors further confirmed rare human cells lacked nucleus-localized GFP/RFP–LMNB1 (Fig. 3C), and immunostaining for human proteins including lamin-A indicates differentiation as a typical epigenetic event of gene regulation rather than reflecting a loss or gain of a chromosome (Fig. S2F). Importantly, flow cytometry showed that the proportion of ChReporter-negative cells increased *in vivo* (Fig. 3D–G, top), ranging from 2- to 30-fold more loss of RFP/GFP–LMNB1 than seen in time-matched and long-term 2D culture controls.

ChReporter-negative cells *ex vivo* were generally out-proliferated by ChReporter-positive cells across most 2D cultures (Fig. 3E–G, lower

Journal of Cell Science (2023) 136, jcs260753. doi:10.1242/jcs.260753

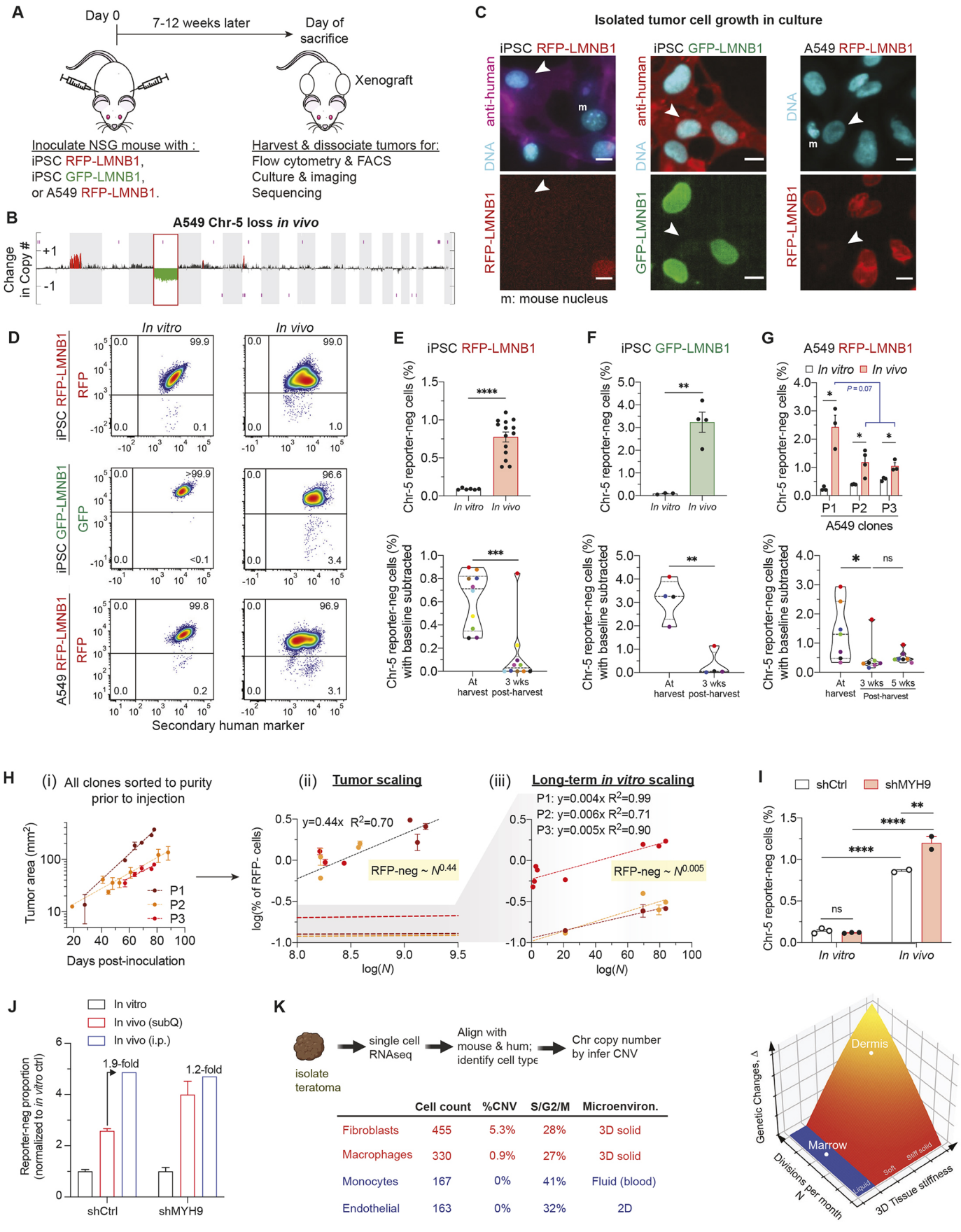

Fig. 3. See next page for legend.

Journal of Cell Science (2023) 136, jcs260753. doi:10.1242/jcs.260753

Fig. 3. Chromosome losses increase in 3D microenvironments *in vivo* with modulation by myosin-II. (A) Human cells were xenografted at subcutaneous sites in immunodeficient NSG mice. Once iPSC teratomas or A549 tumors grew to ∼2 cm diameter, they were harvested, disaggregated and analyzed for Chr-5 reporter loss. (B) SNPa validation of sorted RFP-negative A549 cells confirms ChReporter loss to represent chromosome loss (n=3 tumors). (C) Arrowheads point to nuclei with Chr-5 reporter loss (GFP– or RFP–LMNB1 protein) in 2D cultures (∼1 week) of cells derived from iPSC teratomas (both clones) or from A549 tumors. Anti-human IgG binds human cells, and mouse cells show distinctive chromocenters (m) in Hoechst 33342 staining of DNA. Images representative of at least three repeats. Scale bars: 10 µm. (D–G) Flow cytometry (D) shows increased Chr-5 reporter-negative loss (%) from *in vivo* harvested cells compared to time-matched 2D culture controls for all teratomas and tumors. Quantification (E–G) is for Chr-5 reporter-negative cells from various teratomas or tumors versus *in vitro* cultures, including 3–5-week cultures post-harvest for assessments of persistent viability (n=3–14 replicates). Numbers in D are the percentage of cells in highlighted sector. Top panels in E–G show mean±s.e.m.; bottom panels in E–G are violin plots with median and quartiles marked. *P<0.05; **P<0.005; ***P<0.0005; ****P<0.0001; ns, not significant (unpaired two-tailed t-test with Welch's correction). (H) Tumor growth for all three A549 clones (P1–P3) plotted versus time (i). Log percentage of ChReporter-negative cells plotted versus cell division number (N) (ii). The latter is estimated from tumor size and mean cell volume per confocal imaging of tumors (Fig. 1I). Power-law scaling of Chr-5 reporter-negative A549 cells is much stronger *in vivo* than in 2D cultures (iii), as measured over 200 days with weekly splitting (mean±s.e.m.; n=2–3). (I) Myosin-IIA knockdown iPSCs *in vivo* causes the most Chr-5 reporter-negative cells (RFP–LMNB1) upon disaggregation of solid teratomas (with shMYH9) when compared to *in vivo* controls (shCtrl) or time-matched standard 2D-cultures (*in vitro*) (mean±s.e.m.; n=2–3) **P<0.005; ****P<0.0001; ns, not significant (two-way ANOVA with Tukey's correction for multiple comparisons). (J) Fold-change in ChrReporter-negative cells generated in teratomas (with or without myosin-IIA knockdown) versus corresponding passage-matched 2D controls. All reporter-loss percentages are normalized to the respective 2D control. Stiff teratomas at subcutaneous (subQ) sites show a higher ChReporter-negative proporption with myosin-IIA knockdown, unlike soft teratomas at intraperitoneal (i.p.) sites (error bars indicate n=2–3; mean ±s.e.m.). (K) Normal solid tissue mouse cells exhibit rare and shared chromosome loss or gain based on single-cell RNA-sequencing of teratomas. Freshly isolated teratoma was disaggregated and split for single-cell RNA-seq, with species determined by alignment to reference genomes for human (GRCh38) or mouse (GRCm38). Gene expression profiles were then used for cell type annotation using singleR and copy number from inferCNV (Tickle et al., 2019). Plot on right shows genetic changes increase with divisions and with 3D rigidity of the microenvironment.

plots). Teratoma-derived ChReporter-negative cells mostly died by 3 weeks, with crucial exceptions of viable cells from two teratomas (Fig. 3E,F, bottom). Although iPSCs in 2D cultures seemed intolerant to ChReporter loss (Fig. 1F, bottom), the results with teratoma-derived cells seem consistent with past work showing that some iPSCs can accumulate genetic changes, which limits their application (Mandai et al., 2017). ChReporter-negative A549 cells from tumors also decreased in frequency by 3 weeks of culture but then tended to grow (Fig. 3G, bottom), which is consistent with the robust persistence of abnormal cancer cells. Genetic change under the distinct stresses of 3D is nonetheless highlighted by the uniformly higher percentages of ChReporter-negative cells from freshly harvested teratoma or tumor cells versus 2D cultures. Proliferation under 3D stress *in vivo* is a likely determinant because differences in the percentage of RFP-negative cells between the three A549 RFP–LMNB1 clones (Fig. 3G, top) correlate with the distinct growth rates of the tumors (Fig. 3Hi). Indeed, cell volume estimates from confocal images (Fig. 1D) allowed us to convert measured tumor sizes into total divisions N, yielding a strong power law (Fig. 3Hii,iii):

$$[\%\text{RFP-neg}] \sim N^{a}(a = 0.44\ in\ vivo), \qquad \text{(Eqn. 1)}$$

relative to standard cultures where cells round up and divide unstressed by the overlying fluid

$$[\%\text{RFP-neg}] \sim N^{b}(b = 0.005\ in\ vitro). \qquad \text{(Eqn. 2)}$$

A more general equation for genetic change (Δ) can perhaps be written in terms of a unit 'strain' for confinement (i.e. *strain*=1 for results here) so that larger or smaller strain (or stress) effects in mitosis (e.g. Fig. 2A) might be predicted from:

$$\Delta \sim N^{\wedge}[b + (a - b) * strain]. \qquad \text{(Eqn. 3)}$$

Myosin-IIA knockdown of *LMNB1*-edited iPSCs showed ∼50% more ChReporter loss in teratomas than controls (Fig. 3I), which is consistent with the *in vitro* effects seen upon compression of iPSCs (Fig. 1I). Solid teratoma masses have the same consistency as subcutaneous tumors, which are rich in mouse-derived collagen (Swift et al., 2013). However, intraperitoneal xenografts tend to be larger (Alvey et al., 2017) and lack solidity, and myosin-IIA knockdown shows no increase in ChReporter loss (Fig. 3J). These findings offer insight into how a myosin-IIA knockdown in the stiff dermis of mouse embryo might lead to cancer (Schramek et al., 2014).

To determine whether any mouse cells that have infiltrated in the teratomas also exhibited chromosome copy number variations (CNVs), we applied single cell RNA-seq, using sequence differences to identify various mouse lineages (fibroblasts, endothelial cells and immune cells; see Materials and Methods) and we used a method known as inferCNV to estimate any CNVs in each individual cell. Fibroblasts provide the clearest evidence of CNVs shared across cells (Fig. S2G). Importantly, tissue micro-environments for fibroblasts and macrophages are 3D and matrix-rich and thus likely to confine mitosis, and both lineages showed ∼1–5% of cells with CNVs (Fig. 3K). In contrast, the other two detected lineages showed no CNVs, despite evidence of replication; endothelial cells proliferate in 2D monolayers, which of course implies that they mitotically round up into an overlying fluid, which is similar to what would occur in culture. Past work showing genetic changes in normal tissue has been unclear in terms of lineage specificity, and as such what the effects of 2D versus 3D microenvironments are. Our results thus suggest genetic changes for replicating cells are much lower in soft or fluid tissues versus in stiff 3D tissues, conforming to Eqn 3 but with strain replaced by tissue stiffness.

Inhibiting the spindle assembly checkpoint increases ChReporter loss in 2D culture but not in cells under compression

To assess whether other factors or pathways affect compression results, we studied the effect of inhibitors of the spindle assembly checkpoint (SAC), which controls exit from pro-metaphase in 2D culture (Hiruma et al., 2016, 2015; Santaguida et al., 2010; Skowyra et al., 2018). Chromosome losses and gains in 2D cultures were induced by inhibiting the SAC kinase MPS1, but unlike what was seen for confined mitosis, which causes distention of the spindle (Dumont and Mitchison, 2009) and spreading of mitotic chromatin, MPS1 inhibition (MPS1i) showed no effect on mitotic spreading in 2D culture of A549 cells (Fig. S3A–H). In 2D, MPS1i caused abnormal mitosis as expected (Hiruma et al., 2016; Santaguida et al., 2010) and also caused dose-dependent ChReporter loss (Fig. 4Ai; Figs S1C, S3D). Under compression, surprisingly, MPS1i had no effect on ChReporter loss (Fig. 4Aii), with abnormal mitosis remaining equally high in cells under compression regardless of MPS1i (Fig. 4Aiii). A second drug gave the same results (AZ3146; Fig. 4B), confirming these findings.

Journal of Cell Science (2023) 136, jcs260753. doi:10.1242/jcs.260753

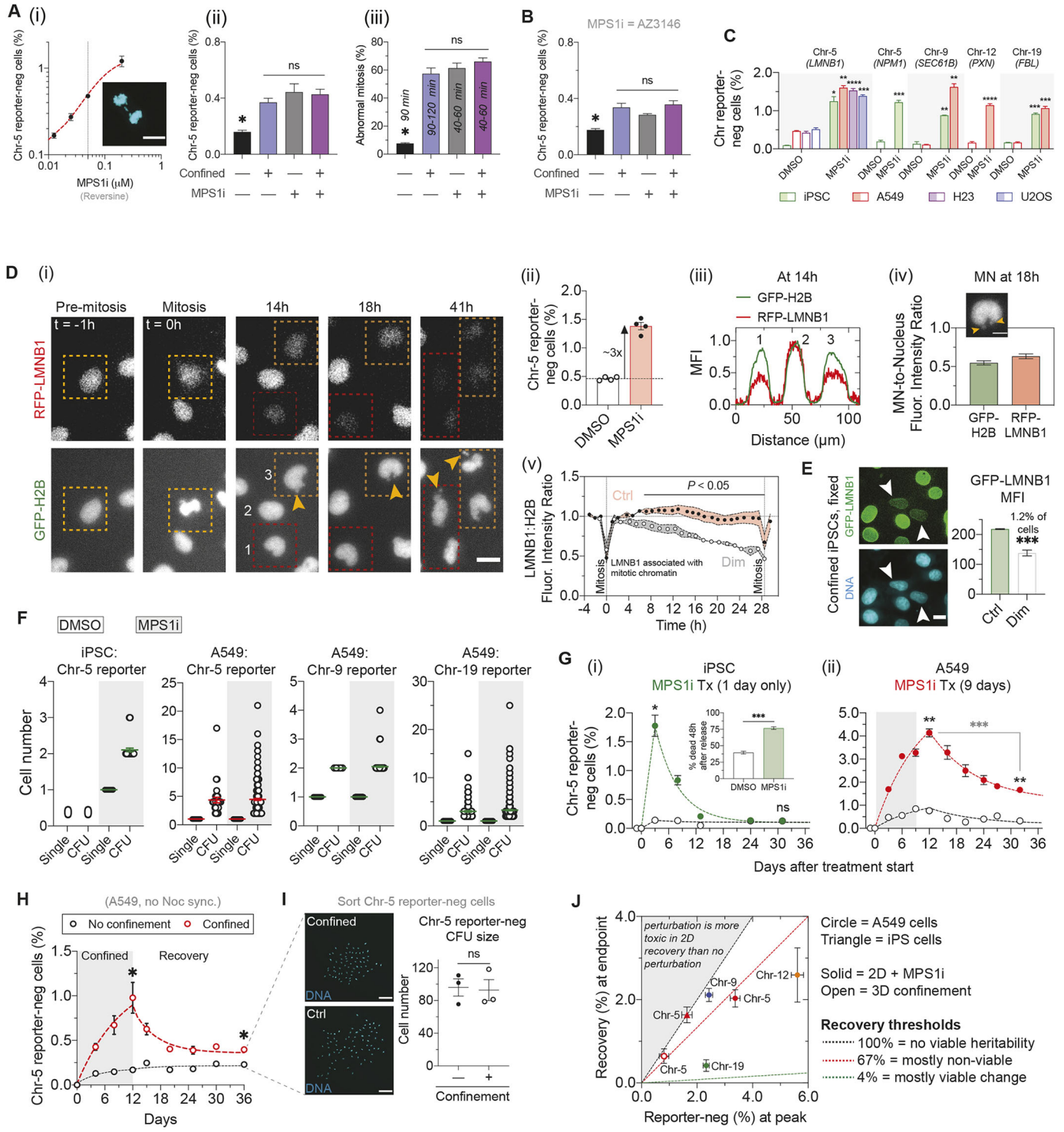

Fig. 4. See next page for legend.

Despite different outcomes in standard 2D culture versus 3D compression, the prolonged mitosis in cells under compression relative to 2D (Dumont and Mitchison, 2009; Lancaster et al., 2013; Matthews et al., 2020) was accelerated by MPS1i to the same extent in 2D and 3D (Fig. 4Aiii; Fig. S3F). This is consistent with what was previously observed upon sustained knockdown of the SAC component MAD2 (Lancaster et al., 2013). One difference with mitotic compression compared to standard 2D culture is that cell death (often in pro-metaphase) is common in compression even without drugs (Figs S2D, S3C). Cell death can be a major fate with some mitosis-perturbing drugs in 2D culture (Huang et al., 2010), and we find MPS1i proves to be fully lethal to compressed iPSCs (data not shown).

At low MPS1i doses that minimize cell death, MPS1i consistently caused ∼1% ChReporter loss, which is similar to compression results for diverse ChReporters and cell types (Fig. 4C). Two distinct Chr-5 ChReporters in iPSCs gave the same results (GFP–LMNB1 and NPM1–RFP; Fig. S1H), and loss of these

Journal of Cell Science (2023) 136, jcs260753. doi:10.1242/jcs.260753

Fig. 4. Compression-driven ChReporter loss is unaffected by inhibition of a '2D' mitotic checkpoint, and colony inheritance of chromosome loss often indicates relatively low viability during 2D recovery. (A) Compressed mitosis has the same effect on ChReporter loss in A549 cells as inhibition of microtubule spindle attachment or signaling with the MPS1 inhibitor reversine (i) Saturable dose–response with MPS1i (n=3 replicates, mean±s.e.m.). Cell image shows anaphase cell with mis-segregation. Scale bar: 10 µm. (ii,iii) Sub-saturating MPS1i (0.1 µM), compression or a combination for 8 h per day over 4 days show the same ChReporter effects (ii), and the same percentage of cells having abnormal mitoses (iii). Time ranges for mitosis indicate MPS1i rescues the prolonged division caused by compression [n=3 replicated, mean±s.e.m., for both (ii) and (iii)]. *P<0.05; ns, not significant (two-way ANOVA with Tukey's correction for multiple comparisons). (B) A second MPS1 drug AZ3146 used at a dose that gives similar ChReporter loss as compression confirms the findings of Aii (n=3 replicates, mean±s.e.m.). *P<0.05; ns, not significant (two-way ANOVA with Tukey's correction for multiple comparisons). (C) ChReporter-negative cells for all engineered lines (iPSCs, A549 and H23 lung adenocarcinoma and U2OS osteosarcoma) treated with MPS1i or DMSO for 3 days. iPSCs expressing GFP–LMNB1 were used in these studies (n=3 replicates, mean±s.e.m.). *P<0.05, **P<0.005, ***P<0.0005; ****P<0.0001 (unpaired two-tailed t-test with Welch's correction). (D) Low-light imaging over 48 h shows (i) A549 cells lose RFP–LMNB1 (expressed from Chr-5) but not GFP–H2B (expressed from Chr-6). Cells treated with a low dose of reversine were treated for 24 h and were then imaged every 20 min. Boxed cells show dimming RFP signal as they divide twice. Scale bar: 20 µm. (ii) Imaging quantification of Chr-5 reporter-negative A549 cells, with a minimum of 2000 cells per well counted. (iii) Intensity profiles across three cells: cells 1 and 3 are RFP-dimming cells, whereas cell 2 remains RFP positive. (iv) Micronuclei (MN) intensity ratios for both RFP–LMNB1 and GFP–H2B. Scale bars: 10 µm. (v) Fluorescence intensity ratio between RFP–LMNB1 and GFP–H2B for RFP-positive control cells and RFP-dimming cells, with intensities normalized to pre-mitosis images. Cell cycles were adjusted to the mean cell cycle time (28.5 h) (mean±s.e.m.; n=3) (unpaired two-tailed t-test with Welch's correction between control and dimming conditions at the same time point: P<0.05). Arrowheads in (i) and (iv) are micronuclei. (E) Imaging of iPSCs (with a GFP tag on *LMNB1*) to identify reporter loss while undergoing mechanical compression. DNA staining is not different between dimming and control cells, but GFP dimming (arrowheads) is consistent with time averages from D (mean ±s.e.m.; n>1000 cells for each condition). ***P<0.0005 (unpaired two-tailed t-test with Welch's correction between control and dimming conditions at the same time point). Scale bar: 10 µm. (F) Cell numbers in reporter-negative cells per colony forming unit (CFU) of iPSCs (with Chr-5 reporter) or A549 cells (with Chr-5, Chr-9 or Chr-19 reporters) when treated with a continuous low dose of reversine or control for 3–5 days. (G–I) The heritable loss model (HLM) fits of Chr-5 reporter-negative kinetics for (Gi) iPSCs or (Gii) A549 cells after MPSi treatment in 2D culture and recovery, or (H) for A549 cells after repeated cycles of rigid compression over 12 days followed by recovery in 2D culture. For the latter, after 36 days, (I) flow-sorted RFP-negative cells from confinement or standard 2D culture were plated back sparsely 1:1 with RFP-positive cells, and RFP-negative cell were imaged and numbers per CFU counted after 1 week; the mixture showed the same total cell numbers for all RFP-positive and -negative samples (n=3 replicates, mean±s.e.m.). *P<0.05, **P<0.005; ***P<0.0005; ns, not significant (unpaired two-tailed t-test with Welch's correction between each treatment condition at the same time point). Scale bar: 100 µm. (J) Heritability of peak loss of reporters plotted against extent of decay from that peak during recovery. Data with statistics are from experiments shown in G,H and similar for other ChReporter cells.

edited chromosomes also caused loss of heterozygosity (LOH), which proves that there is DNA sequence change (Fig. S1H, purple ticks). With ChReporters edited into two chromosomes, loss of both proved to be rare in A549 cells but common in iPSCs (Fig. S3J), consistent with the many changes seen in the single-cell DNA-seq results (Fig. S1C).

To further assess perturbations of compressed mitosis, mitotic cells were arrested by inhibiting cyclin-B degradation (Brito and Rieder, 2006). Surprisingly, such inhibition has no effect on the protracted mitotic exit in compression but did suppress anaphase and ChReporter loss (Fig. S3I). A tentative conclusion is confinement-induced chromosome loss requires mitotic exit via anaphase.

Live imaging over days showed *de novo* ChReporter loss and direct evidence of heritability in viable colonies (Fig. 4D). Importantly, this rules out selection under compression of pre-existing rare cells. Image analysis of >1000 cells confirmed the ∼3-fold increase in RFP–LMNB1 loss with MPS1i (per Fig. 4A; using low illumination to minimize photobleaching and DNA damage). Nuclear envelope breakdown in mitosis led to the expected dispersal of RFP–LMNB1, which then was diluted through progressive divisions (Fig. 4D). In iPSCs after compression, GFP–LMNB1 showed a similar dimming in ∼1% of cells (Fig. 4E), but the number of cells per colony forming unit (CFU) was much lower for iPSCs than for A549 cells after the same interval (Fig. 4F), even though iPSCs normally divide faster. Aneuploidy is common in early animal development but aneuploid cells robustly die (Eggan et al., 2002).

Micronuclei in our images (Fig. 4D, arrows) provide a signature of mis-segregated chromosomes, and the micronuclei often accumulate DNA damage when lamin-B is low (Umbreit et al., 2020) and curvature is high (Xia et al., 2019). Our measurements showed lamin-B is not depleted relative to DNA in micronuclei within A549 cells (Fig. 4Div), suggesting that they have low DNA damage. A549 cells showed more micronuclei post-compression than iPSCs. This could reflect near-zero tolerance of iPSCs to chromosome loss in 2D culture without MPS1i (Fig. 1F,I; Fig. 3E, F), and the many MPS1i-induced chromosome losses or gains evident after only a few days (Fig. S3D) subsequently disappear after withdrawing the drug (Fig. 4Gi).

Cycles of confined mitosis show that losses scale with divisions, but death limits heritability

Various ChReporter A549 cells in 2D showed basal loss of ChReporters in colonies even after 2 weeks, and MPS1i for 9 days not only tended to increase the proportion of ChReporter-negative cells and colonies, but drug withdrawal also led to variable levels of viable cells with sustained ChReporter loss (Fig. 4Gii). Importantly, compression-generated ChReporter-negative A549 cells behave similarly: once compression cycles are stopped by switching to standard 2D culture, the proportion of ChReporter-negative cells diminished to a level above controls (Fig. 4H). Further culturing showed that RFP-negative cells from all conditions exhibited heritable loss, as equally large, viable colonies were found regardless of ChReporter loss in compression or in standard 2D culture (Fig. 4I). The results are consistent with there being *de novo* genetic diversification under mitotic compression and MPS1 inhibition, but also further stressor effects on subsequent selection (Fig. 4J).

Mathematically, a heritable loss model (HLM) accounts for ChReporter loss rate and proliferation (Fig. 5A), indicating slower net proliferation after loss (7% to 47%). Compression and MPS1i accelerate Chr-5 loss by ∼4-fold relative to controls. The HLM also accommodates power laws for ChReporter loss versus the number of divisions (N) (Fig. 5B), as applied *in vivo* (Fig. 3H). For 2D cultures where stiffness E=0 for the overlying fluid phase, ChReporter loss $\Delta{\sim}N^a$ gives a∼0.03 to 0.1 (i.e. weak scaling). For rigid compression ($E >> 0$) and for MPS1i perturbations, $\Delta{\sim}N^b$ with b/a∼2.5. The modeling consistently shows stress-driven acceleration of chromosome loss (by ∼2 to 10-fold), and growth or viability in 2D further shows chromosome- and cell-type-specific differences.

Journal of Cell Science (2023) 136, jcs260753. doi:10.1242/jcs.260753

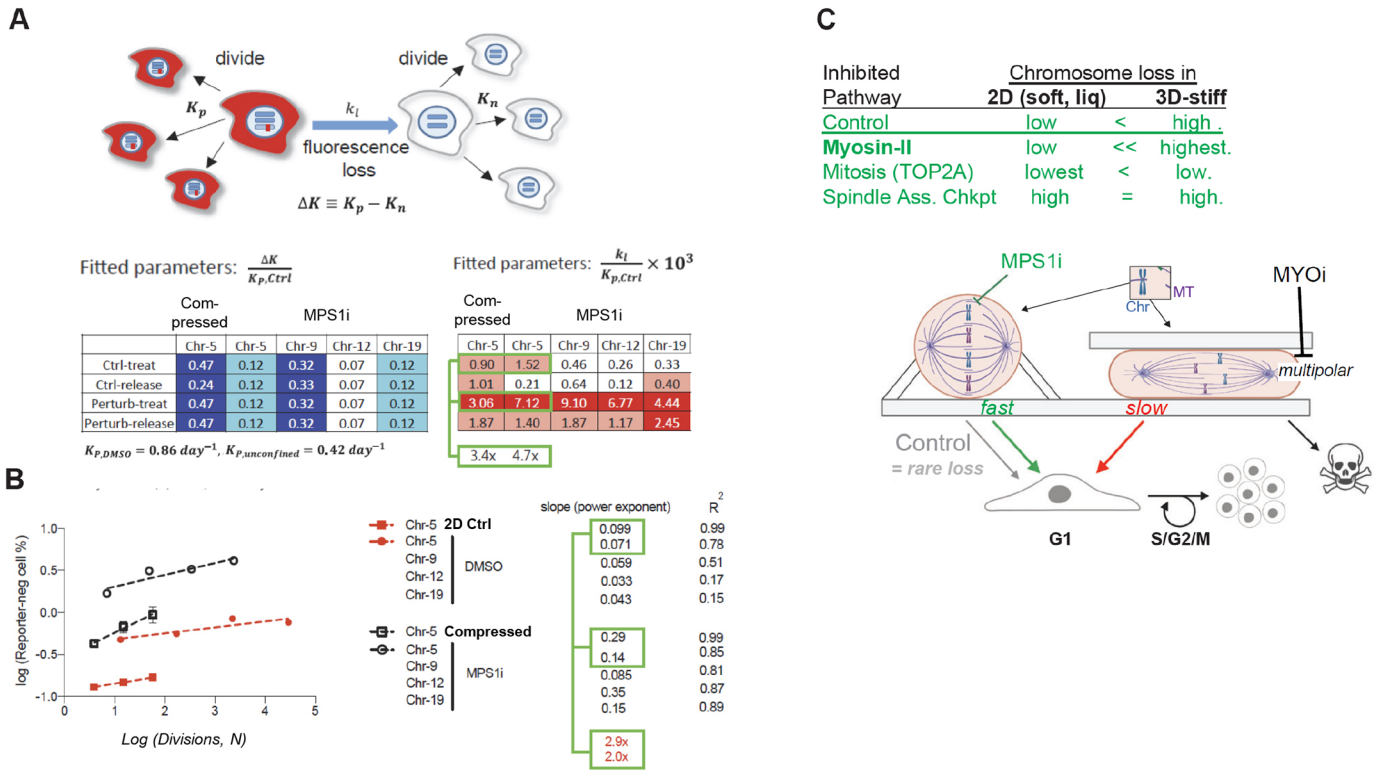

Fig. 5. Mathematics of a heritable loss model for ChReporter loss kinetics, including power-law scaling with cell division, and compression-dependent pharmacology. (A) Schematic showing cell division and fluorescence loss, with K_p, K_n, k_l respectively quantifying net proliferation of reporter-positive cells, net proliferation of reporter-negative cells, and fluorescence loss rate. The latter is then derived as $r(t)$ (see Materials and Methods). Fitting parameters are normalized to the fixed value $K_{p,Ctrl}$ (Fig. 4G,H). We assume ΔK is identical for all the phases except for the MPS1i treatment phase. For each reporter $k_{l,\ Perturb} > k_{l,\ Ctrl}$, which is consistent with increased chromosome loss. (B) Power-law scaling of all ChReporters during MPS1i treatment as well as for Chr-5 reporter under compression. The perturbed processes have steeper slopes than their corresponding controls, with fold changes of 1.5 to 10. Linked green boxes in A and B highlight the fold changes from upper boxes to lowest boxes in each panel. (C) ChReporter loss in 2D versus compression or confinement for various pathways. Myosin-IIA inhibition has no effect in 2D but increases loss in confinement. MPS1i only affects 2D culture, and gives results similar to confinement, perhaps by limiting microtubule attachment or signaling. In all cases some viable, cycling cells show heritable loss. MT, microtubule.

DISCUSSION

Mechano-evolution can be driven by confined mitosis, which causes viable genetic diversity rather than just cell death or senescence. Suppression of the putative 'tumor suppressor' myosin-II amplifies confinement-induced chromosome loss but has no effect in standard 2D culture (Fig. 5C) despite previous speculation (Booth et al., 2019; Ma et al., 2010; Rosenblatt et al., 2004; Taneja et al., 2020). Cell division is necessary but not sufficient for chromosome loss based on Etop-mediated inhibition of mitosis. Surprisingly, however, SAC inhibition increases chromosome loss only in 2D culture, suggesting that confinement perturbs the SAC or else perhaps the combination is lethal.

The mono-allelic ChReporter approach is broadly applicable to cell biology, as there is visible proof of viable growth of rare cells. Hence, evolutionary selection via death or senescence versus colony formation need not be merely inferred from standard genetic methods that require killing cells, that lack spatial information and sensitivity to 1% or fewer cells, or that are limited to hundreds of cells as per single-cell sequencing (e.g. Fig. 1C; Fig. S1). Despite the latter limitations, we did find that normal unedited mouse tissue cells show rare losses or gains of chromsosomes only within 3D stiff microenvironments, but not soft or liquid microenvironments. Such a finding is consistent with our ChReporter results.

Confinement and compression effects could relate to proposed effects of abnormal tissue architecture via integrins (Knouse et al., 2018), particularly if abnormal architecture somehow leads to a stiffer microenvironment. Understanding any relationship will probably benefit from determinations of the maximum and minimum compression as well as the ligand densities required to initiate chromosome instability and loss while maintaining viability. It will be equally interesting to drive more cell division in cells and particularly cells interacting within a soft environment, but it should be noted that iPSCs divide several-fold faster than typical cancer lines and yet give similar results (Fig. 1F). Suppression of actomyosin and its connections to integrin adhesions generally causes dysregulation of interphase mechanosensing (Engler et al., 2006; Meng et al., 2018; Nava et al., 2020; Paszek et al., 2014; Petridou et al., 2021; Przybyla et al., 2016; Segel et al., 2019; Uhler and Shivashankar, 2017), and the finding that myosin-II suppression also limits centriole splitting (Vitiello et al., 2019) provides a mechanistic explanation for its rescue of 'lethal' multipolar divisions in favor of the more-viable mis-segregations (Figs 2D, 5C). Regulation of p53 by myosin-IIA might cause the presumed genetic changes that lead to cancer with myosin-IIA suppression (Schramek et al., 2014), but such p53 regulation remains unclear (Conti et al., 2015). Non-muscle myosin-II depletion in a cardiomyocyte tumor line also increases MT acetylation-mediated stabilization as well as abnormal mitosis and cell death in 2D cultures (Ma et al., 2010), and the MT effects have been linked not only to a phosphatase that inhibits contractility and a MT-targeting de-acetylase (Joo and Yamada, 2014) but also to breast cancer aneuploidy (Sudo, 2018), which seems consistent with our findings.

Journal of Cell Science (2023) 136, jcs260753. doi:10.1242/jcs.260753

Mitotic compression certainly distorts the MT spindle and increases chromosome mis-segregation (Brito and Rieder, 2006; Dumont and Mitchison, 2009; Lancaster et al., 2013), but the unexpected lack of importance of the MT-engaging SAC during 3D compression seems to align with the fact that SAC genes, such as *MPS1*, are rarely identified as tumor suppressors, including an in-depth analysis of tumor suppressors in chromosome losses across 21 tumor types (Davoli et al., 2013). SAC genes are also not identified in screens that show 3D spheroids are better than 2D cultures in revealing growth effects of '3D' oncogenes and '3D' tumor suppressors, whereas myosin-IIA knockout led to increased growth and thus suggested tumor suppressor activity (Han et al., 2020). However, growth is insufficient for genetic changes as required for cancer, and molecular mechanisms of genetic change might be understood more deeply through use of ChReporters.

MATERIALS AND METHODS

Cell lines and culture

The cancer cell lines used in this study were: A549 lung adenocarcinoma, U2OS osteosarcoma, and NCI-H23 lung adenocarcinoma (referred to as H23 in text). The A549 and U2OS cell lines were obtained from the American Type Culture Collection (ATCC). The H23 cell line was a gift from Dr Michael C. Bassik (Stanford University, CA, USA). A549 cells were cultured in Ham's F-12 medium (Gibco 11765047); U2OS cells in DMEM (Gibco, Catalog no. 10569010); and H23 cells in RPMI 1640 (Gibco, Catalog no. 11879020). The A549 RFP–LMNB1 cell line was described previously (Pfeifer et al., 2018). HEK293T cells from ATCC were used for lentiviral packaging and cultured in DMEM. All aforementioned cell lines were cultured in media supplemented with 10% (v/v) fetal bovine serum (FBS; MilliporeSigma, Catalog no. F2442) and 100 U ml^{-1} penicillin-streptomycin (Gibco, Catalog no. 15140122). All cells were passaged every 2–3 days using 0.05% trypsin-EDTA (Gibco, Catalog no. 25300054). All cell lines were incubated at 37°C and maintained at 5% CO_2.

The following induced pluripotent stem cell (iPSC) lines were also used, all of which were acquired from the Coriell Institute for Biomedical Research and generated and/or validated by the Allen Institute for Cell Science: AICS-0013 cl.210, AICS-0059 cl.36, and AICS-0084 cl.18. iPSCs were cultured in mTseR Plus medium (STEMCELL Technologies, Catalog no. 05825), with mTser Plus 5X supplement and 100 U ml^{-1} penicillin-streptomycin. For passaging and maintenance of iPSCs, cells were lifted with accutase (Sigma, Catalog no. A6964) at 37°C and re-plated into 10-cm plates (Corning) coated with Matrigel (Corning, Catalog no. 356231) following the Allen Institute of Cell Science's protocol (Roberts et al., 2017). 10 mM ROCK inhibitor (Y-27632; STEMCELL Technologies, Catalog no. 72302) was added to replated cultures to help with adherence and to prevent differentiation. Passaging was performed once iPSC cultures reached 70% confluency to prevent spontaneous differentiation. All iPSC lines were also cultured at 37°C and maintained at 5% CO_2.

Monoallelic chromosome tagging

All knock-in reporter lines were generated following the protocol established in using CRISPR/Cas9 technology (Roberts et al., 2017). Donor plasmids were designed such that unique designs for each target locus contain 5′ and 3′ homology arms (1 kb each) for the desired insertion site, based on the GRCh38 reference human genome. For all attempted monoallelic chromosome reporters as described in Fig. 1E, donor constructs were: AICSDP-8:TOMM20-mEGFP (Addgene plasmid #87423), AICSDP-13:FBL-mEGFP (Addgene plasmid #87427;), AICSDP-35: AAVS1-mEGFP (Addgene plasmid #91565), AICSDP-42:AAVS1-mTagRFPT-CAAX (Addgene plasmid #107580), AICSDP-1:PXN-EGFP (Addgene plasmid #87420), AICSDP-10:LMNB1-mEGFP (Addgene plasmid #87422), AICSDP-52: HIST1H2BJ-mEGFP (Addgene plasmid #109121), AICSDP-7:SEC61B-mEGFP (Addgene plasmid # 87426).

For editing, we use the ribonucleic protein (RNP) method with recombinant wild-type *Streptococcus pyogenes* Cas9 protein pre-complexed with a synthetic CRISPR RNA (crRNA) and a trans-activating crRNA (tracrRNA) duplex. Recombinant wild-type Cas9 protein was purchased from the University of California–Berkeley QB3 Macrolab, while crRNA and tracrRNA oligonucleotides were designed by and purchased from Horizon Discovery. For transfection of donor templates into target cells, we used the electroporation using a Gene Pulser Xcell Electroporation System (Bio-Rad). 700,000 target cells were lifted using 0.05% trypsin-EDTA, resuspended in 200 µl of fresh medium without penicillin-streptomycin, and loaded into a 0.4-cm cuvette. 4 µl of both 10 µM crRNA:tracrRNA duplex and 10 µM recombinant Cas9 protein were added to the cell solution, as well as 8 µg of donor plasmid. Electroporation conditions were as follows: (1) A549 and H23: 200 V with 45 ms pulse length using a square-wave protocol; (2) U2OS: 160 V with 30 ms pulse length using a square-wave protocol. After electroporation, cells were allowed to expand for ∼1 week and then enriched via fluorescence-activated cell sorting (FACS), as described below. Three to five FACS enrichment cycles were performed to achieve a pure reporter-positive population.

Single-cell CNV-sequencing and analysis

A549 cells from RFP-positive clone-3, RFP-negative clone-1 and RFP-negative clone-2 were plated in a 24-well plate at 60,000 cells per well and cultured for 2 days. RFP-positive clone-3 was used as the reporter-positive sample, and a 1:1 mixture of the two reporter-negative clones served as the overall reporter-negative sample. The DNA library was constructed using the Chromium Single Cell CNV kit from 10X Genomics (PN-1000041, Pleasanton, CA) per the manufacturer's instructions. The libraries were submitted to the University of Pennsylvania's Next Generation Sequencing Core (12-160, Translational Research Center, University of Pennsylvania) for sequencing using HiSeq 4000, 150 bp paired-end from Illumina (San Diego, CA). For each sample, the copy number data was generated using Cell Ranger DNA pipeline (10X Genomics) and was visualized using Loupe scDNA Browser (10X Genomics). Cells that were flagged as 'noisy' by the Cell Ranger pipeline were removed from further analysis. Cells with more than 69 copies of chromosomes were removed from the CNV analysis to avoid potential influence of cell cycle effects. Built-in hierarchical clustering from 10X Genomics was also used to rearrange the cells.

Single cell RNA-sequencing

RNA libraries were constructed using the Chromium Single Cell Gene Expression kit (v3.1, single index, Catalog no. PN-1000128; PN-1000127; PN-1000213) from 10X Genomics per the manufacturer's instructions. The libraries were submitted to the University of Pennsylvania's Next Generation Sequencing Core for sequencing using NovaSeq 6000 (100 cycles) from Illumina. Raw base call (BCL) files were analyzed using CellRanger (version 5.0.1) to generate FASTQ files and the 'count' command was used to generate raw count matrices aligned to GRCh38 provided by 10X genomics. For teratoma samples, FASTQ files were aligned to both GRCh38 and GRCm38. The cells are labeled to be human/mouse cells if more than 90% of the sequence is aligned to GRCh38/GRCm38. The data generated was imported as a Seurat object (4.0.0) for future downstream analysis (Stuart et al., 2019). Cells were filtered to make sure that they expressed 500 and 6000 genes inclusive and had less than 10 percent mitochondrial content. Data was normalized using the 'LogNormalize' method or sctransform package (0.3.2) (Hafemeister and Satija, 2019). Differential expression analysis was performed using the 'FindAllMarkers' command and the output was used for the volcano plot. The very first 30 dimensions were used to generate a UMAP. Cell cycle analysis was performed using 'CellCycleScoring' command.

InferCNV analysis

Raw expression matrices from Seurat (4.0.0) were imported to create inferCNV object (1.7.1) (inferCNV of the Trinity CTAT Project, https://github.com/broadinstitute/inferCNV). Gene position files were created for GRCh38. The default hidden markov model (HMM) was used to confirm the validity of CNVs discovered. A Bayesian latent mixture model was then implemented to calculate the possibility of having a different copy number state from the results of HMM prediction. Low probability CNVs were filtered if the CNV region has a more than 20% chance of being normal (default value is 50%) (Tickle et al., 2019).

Cell type annotations

Raw expression matrices were used as the input for the singleR (1.4.1) package (Aran et al., 2019). The cell types were annotated based on Human Primary Cell Atlas (Mabbott et al., 2013).

Karyotyping

Cells used for karyotyping were plated in T25 flasks (Corning) and cultured for 2–3 days to reach ∼50% confluency. The medium was then discarded and replaced with fresh medium to fill the entire flask with a closed lid, after which the flask was wrapped with parafilm. The samples were then sent to Cell Line Genetics (Madison, WI) for metaphase-spread karyotyping.

PCR for reporter validation

DNA was extracted as previously described for SNP arrays (SNPa). The isolated DNA was then mixed with materials from KAPA HiFi PCR Kit (Roche, Catalog no. 07958838001) to start each PCR reaction. Each reaction contains 5 µl 5× HiFi Fidelity Buffer, 0.75 µl 10 mM KAPA dNTP Mix, 0.5 µl 1 U/µl KAPA HiFi DNA Polymerase, 0.75 µl of 10 µM forward and reverse primers, respectively, and 1 ng of extracted DNA template. PCR grade water was then filled up to 25 µl. All materials suggested by the kit were placed on ice prior to mixing. The reaction mix was placed on the thermocycler with the following temperature cycling protocol: Initial denaturation at 95°C for 3 min; 35 cycles of denaturation at 98°C for 20 s, annealing at 65°C for 15 s, extension at 72°C for 60 s/kb; and final extension at 72°C for 1 min. All PCR products were then run on a 1% (v/v) agarose (Invitrogen, Catalog no. 16500500) gel at 100 V for 1 h and then imaged using a ChemiDoc MP Imaging System (Bio-Rad, Catalog no. 17001402).

Reporter validation via single-nucleotide polymorphism arrays and analysis

Genomic DNA was isolated from a minimum of 3.0×10^5 cells with the Blood & Cell Culture DNA Mini Kit (Qiagen, Catalog no. 13323) as per the manufacturer's instructions. In the event that cells were either very rare (such as reporter-negative cells) or had poor viability after FACS enrichment (specifically, iPSCs), genomic DNA was amplified post-extraction using the Illustra Single Cell GenomiPhi DNA Amplification Kit (GE Healthcare Biosciences, Catalog no. 29108107) following the manufacturer's instructions. All DNA samples were sent to The Center for Applied Genomics Core in The Children's Hospital of Philadelphia, PA, for single nucleotide polymorphism SNP array HumanOmniExpress-24 BeadChip Kit (Illumina) analysis. For this array, >700,000 probes have an average inter-probe distance of ∼4 kb along the entire genome. For each sample, the Genomics Core provided the data in the form of GenomeStudio files (Illumina). Chromosome copy number and LOH regions were analyzed in GenomeStudio by using cnvPartition plug-in (Illumina). Regions with one chromosome copy number are not associated with LOH by Illumina's algorithm. Hence, regions with one chromosome copy number as given by the GenomeStudio are added to the LOH region lists. SNPa experiments also provide genotype data, which was used to give single nucleotide variation (SNV) data. In order to increase the confidence of LOH data given by the GenomeStudio, the changes in LOH of each chromosome from each sample were cross referenced to their corresponding SNV data. Data extracted from GenomeStudio was analyzed with MATLAB scripts (available upon request).

Lentiviral packaging and delivery

MYH9 silencing was performed by lentiviral-driven expression of short-hairpin RNAs purchased from Sigma-Aldrich, using the pLKO backbone construct. The following shRNAs were used: TRCN0000285480, TRCN0000029468, TRCN0000029466, TRCN0000276055 and TRCN0000276070. For non-targeting shRNA control, the pLKO-sh-HSC plasmid was used (Addgene plasmid #46896). Lentivirus was produced in HEK293T cells using MirusBio TransIT-Lenti Transfection Reagent (Catalog no. MIR 6604) following the manufacturer's protocol. Lentiviral production was allowed to occur for 48 h, after which the supernatant was collected. Lentivirus was concentrated and purified from traces of fetal bovine serum using the PEG-it Virus Precipitation Solution (System Biosciences, Catalog no. LV810A-1) following the manufacturer's protocol. Infected cells were selected by incubation using 1 µg ml^{-1} puromycin (Corning, Catalog no. 61385RA).

Transfection

All siRNAs used in this study were purchased from Dharmacon (ON-TARGETplus SMARTpool siBRCA1, L-003461-00; siBRCA2, L-003462-00; siKu80, L-010491-00). A549 cells were passaged 24 h prior to transfection. An siRNA pool (25 nM each) with 1 µg/ml Lipofectamine 2000 (Thermo Fisher Scientific, Catalog no. 11668-030) was prepared according to the manufacturer's instructions, added to cells, and allowed to incubate for 3 days. Knockdown efficiency was determined by immunoblotting following standard methods as described in Xia et al., (2019). For overexpression of TOP2A, the pBL-Puro EGFP-TopoIIA plasmid was a kind gift from Dr Andrew Porter (Imperial College London, UK) and was transfected into U2OS osteosarcoma cells using Lipofectamine 2000. Confirmation of overexpression and monitoring of cell viability was undertaken via microscopy using an Olympus IX inverted microscope with a 40×/0.6 NA or 20×/0.4 NA objective using a sCMOS camera (Photometrics Prime).

Treatments

For all cancer cell treatments, either 300,000 cells were plated per well in a 6-well plate (Corning) (e.g. Fig. 2A) or 60,000 cells per well in a 24-well plate (Corning). For iPSC treatments, 60,000 cells were plated per 6-well plate. The following chemical treatments were used: MPS1 inhibitor reversine (Cayman Chemical, Catalog no. 10004412), MPS1 inhibitor AZ3146 (Cayman Chemical, Catalog no. 19991), TOP2A inhibitor etoposide (Cayman Chemical, Catalog no. 12092), nocodazole (MilliporeSigma, Catalog no. M1404), blebbistatin [MilliporeSigma, Catalog no. 203389; some experiments with similar results used the more photostable para-amino-blebbistatin (Cayman, CAS no. 2097734035)], GSK-3 inhibitor CHIR-99021 (MilliporeSigma, Catalog no. SML1046), and dimethyl sulfoxide (DMSO; Millipore Sigma, Catalog no. D2438). The reversine concentrations and treatment times used, unless otherwise stated, are: for A549 cells, 0.1 µM for 72 h; for U2OS and H23, 1.5 µM for 24 h followed by washout and 48 h recovery; for iPSCs, 0.25 µM for 24 h followed by washout and 24–48 h recovery. All AZ3146 treatments were done at 1.5 µM for 24 h followed by washout and 48 h recovery. Non-confinement etoposide studies were done at 1 µM for 24 h followed by washout and 48 h recovery. For myosin-IIA inhibition studies, blebbistatin was used at 20 µM for 24 h followed by washout and 48 h recovery or used at the same concentration for the entire of a confinement session. For all cell-cycle synchronization, nocodazole was added to cells at a final concentration of 50 ng ml^{-1} for 12–18 h. For reversine treatments paired with either nocodazole or confinement, only a 50 nM concentration was used.

Flow cytometry and FACS

All flow cytometry was performed on a BD LSRII (Benton Dickinson) and analyzed with FCS Express 7 software (De Novo Software). All studied cell lines were detached by brief trypsinization (for all cancer lines in 2D culture) or with accutase (for iPSCs and 3D-spheroids), washed, and resuspended in FACS buffer (PBS plus 5% FBS) with 1.0 µg ml^{-1} DAPI (MilliporeSigma, Catalog no. 09542). For all dissociated tumor and teratoma xenograft quantification of reporter-negative subpopulations, dissociated cells were washed and resuspended in PBS plus 5% (v/v) BSA containing mouse BD Fc Block (Clone 2.4G2; BD Biosciences, Catalog no. 553141) at a 1:500 dilution of the stock. Cell suspensions were incubated at 4°C for 30 min and agitated occasionally to prevent cell settling. Once the 30-min incubation period elapsed, anti-human IgG (Rockland Immunochemicals, Catalog no. 109-4139) was spiked into the FACS buffer for a final 1:500 dilution. Cell suspensions were again incubated at 4°C for 30 min and agitated occasionally to prevent cell settling. Cells were then washed twice with FACS buffer and incubated with a 1:500 dilution of donkey anti-rabbit-IgG AlexaFluor 647-conjugated secondary antibody against the anti-human IgG

in FACS buffer for 30 min at 4°C. Finally, cells were washed twice and resuspended in FACS buffer containing 1.0 µg ml^{-1} DAPI. For fluorescence-activated cells sorting (FACS), cells were prepared in the same way as described above except that freshly prepared sterile FACS buffer was used and no DAPI was included. FACS was performed on either a BD FACS Aria II or a BD FACS Jazz machine. Prior to any assay that assessed reporter-negative subpopulation generation, cells were FACS-enriched for only reporter-positive cells. Cultures were also routinely FACS-enriched every 2 weeks to remove spontaneous, naturally occurring aneuploid reporter-negative cells.

For gating, forward scatter parameters FSC-A versus FSC-H and side scatter parameters SSC-A versus SSC-H were used to remove aggregates from analysis. Live cells were gated on using forward scatter and side scatter (FSC-A versus SSC-A). DAPI was further used to discriminate between live cells and debris or dead cells. For tumor and teratoma flow cytometry quantification, additional gates were added to remove mouse cells from human xenograft samples. Only anti-human IgG-high cells were gated on. In the case of teratomas, when possible, a secondary GFP-SEC61B marker unique to the human iPSCs was also used to further remove any potential mouse cell contaminants in the analysis.

Antibodies

In addition to antibodies previously described for flow cytometry, additional antibodies used in this study are as follows: anti-LMNB1 (Abcam, Catalog no. ab16048), anti-RFP (Rockland, Catalog no. 200-101-379), anti-alpha/beta-tubulin (Cell Signaling Technology, Catalog no. 2148S), anti-myosin-IIA (Cell Signaling Technology, Catalog no. 3403S), anti-TopoIIalpha (Santa Cruz Biotechnology, Catalog no. sc-365916), and AlexaFluor 647 donkey anti-mouse-IgG (H+L) secondary (Invitrogen, Catalog no. A31571). Western blotting used ECL anti-mouse-IgG horseradish peroxidase (HRP)-linked whole antibody (Cytiva, Catalog no. NA931V) and ECL-anti-rabbit-IgG HRP-linked whole antibody (Cytiva, Catalog no. NA934V).

Immunoblotting

Western blotting was performed using standard methods. In brief, cells were briefly trypsinized, washed three times with cold PBS, and then lysed in RIPA buffer (150 mM NaCl, 1% NP-40 alternative, 0.5% sodium deoxycholate, 0.1% SDS, 40 mM Tris-HCl pH 8.0) containing 1× protease inhibitor cocktail (Sigma, Catalog no. P8340), followed by centrifugation to discard lipids and some nucleic acids, and boiled in 1× NuPage LDS sample buffer (Invitrogen, Catalog no. NP0007) with 2.5% (v/v) β-mercaptoethanol. Approximately 1.0×10^6 cells were used for each analysis. Proteins were separated by electrophoresis in NuPAGE 4–12% Bis-Tris gels run with 1× MOPS buffer (Invitrogen, Catalog no. NP0323), or 3–8% Bis-Tris gels run with 1× Tris-acetate buffer (Invitrogen, Catalog No. LA0041, Myosin IIa only) and transferred to an iBlot nitrocellulose membrane (Invitrogen, Catalog no. IB301002). The membranes were cut into strips corresponding to one lane loaded with lysate and one lane loaded with a molecular mass marker and then blocked with 5% non-fat milk in Tris-buffered saline (TBS) plus 0.1% Tween-20 (TBST) for 1 h. The membranes were washed with TBST and incubated with 1:500 secondary antibody conjugated with horseradish peroxidase in 5% milk in TBST for 1 h at room temperature with agitation. The membranes were washed again with TBST, then TBS, and developed with a 3,3′,5,5′-teramethylbenzidine (TMB) substrate (Genscript L0022V or Sigma T0565). Developed membranes were scanned and analyzed with ImageJ (National Institutes of Health).

Immunofluorescence and imaging

Cells were fixed in 4% formaldehyde (Thermo Fisher Scientific, Catalog no. 28908) for 15 min, followed by permeabilization by 0.5% Triton-X (MilliporeSigma, Catalog no. 112298) for 15 min, and blocked with 5% bovine serum albumin (BSA; MilliporeSigma, Catalog no. A7906) for 30 min and overnight incubation in primary antibodies (1:500 dilution). The cells were then incubated in secondary antibodies (1:500 dilution) for 1.5 h, and their nuclei were stained with 8 µM Hoechst 33342 (Thermo Fisher, Catalog no. 62249) for 15 min. When mounting is involved, Prolong Gold antifade reagent was used (Invitrogen, Catalog no. P36930). Micronucleated cells were classified manually by distinct staining by Hoescht 33342 of structures outside of the main nucleus. Epifluorescence imaging was performed using an Olympus IX71 with a digital camera (Photometrics) and a 40×/0.6 NA objective. For certain samples, confocal imaging was performed on a Leica TCS SP8 system with a 63×/1.4 NA oil-immersion. Live imaging was done on an EVOS FL Auto Imaging System with 10× or 20×/0.6 NA object in standard culture conditions (37°C, 5% CO_2, complete culture medium per above).

MPS1 inhibition kinetics and CFU studies

For MPS1i studies, A549 cells were originally plated at a density of 30,000 cells per 24-well after FACS enrichment for reporter-positive cells and then treated with 0.1 µM reversine continuously for 9 days. Cells were then allowed to recover for 3–4 weeks. Cells were passaged whenever they approached ∼80% confluency (every ∼3 days) and a sample of the passaged population was analyzed via flow cytometry. Whenever cells were passaged within the first 9 days, they were replated in fresh media with reversine.

For all colony-forming units (CFU) studies, A549 cells were continuously treated with 0.1 µM for 3–5 days to allow for generation of identifiable reporter-negative CFUs. Cells were plated at a low density (∼20,000 cells per well in 6-well plates) to avoid passaging in the allotted time frame. For iPSCs, cells were treated with reversine following the previously described treatment. CFUs were identified via microscopy using an Olympus IX inverted microscope with a 40×/0.6 NA or 20×/0.4 NA objective and equipped with a sCMOS camera (Photometrics Prime). Images were quantified using ImageJ software.

In vitro mechanical compression assays

Prior to all mechanical confinement assays, A549 cells were FACS-enriched for reporter-positive cells only, as described in the 'Flow cytometry and FACS' section. iPSCs did not have to be FACS-enriched, as these cultures usually maintained below a 0.1% reporter-negative population even after continuous culture for ∼1 year, suggesting genomic stability. The night prior to assay, 30-mm glass coverslips were coated with RainX (glass water repellent PDMS; RainX Company, Catalog no. 1597562) and then left in PBS under ultraviolet light for sterilization overnight. For assay, A549 cells were plated at 300,000 cells per well in 6-well plates. Roughly 24 h later after which cells had settled and adhered, they were treated with nocodazole at a concentration of 50 ng ml^{-1} to allow for synchronization. At the same time, 6.58-µm polystyrene beads (SpheroTech, Catalog no. SVP-60-5) were added at the same density as the cells during this time. These polystyrene beads served as spacers to control the height of mechanical confinement and would also adhere to the cell culture plastic after the synchronization time period. After 12-18 h of nocodazole synchronization, cells were gently washed five times with PBS and then replenished with 1.5 ml of fresh medium. Then, sterile, RainX (PDMS)-coated 30-mm glass coverslips were gently placed on top of the cells. A sterilized, stainless-steel weight was then placed on top of the coverslip to complete confinement. The complete confinement setup (stainless-steel weight with PDMS-coated glass coverslip) was removed after 8–10 h, cells were gently washed with PBS, and fresh medium was added to the recently confined cultures. Cells were allowed to grow for 2 days before brief trypsinization and flow cytometry quantification of the generation of reporter-negative cells. A subset of these cells was also plated back for repeated confinement cycles as necessary. Etoposide studies (Fig. 2C) followed the synchronization protocol, and the drug was added only during confinement, and washed out afterwards.

All iPSC and non-nocodazole synchronized A549 confinement studies followed the same exact procedure as the original nocodazole-synchronized A549 experiment (as above) with the exception of nocodazole synchronization. iPSCs were plated at 600,000 cells per well in 6-well plates, while A549 cells were still plated at the original density. Roughly 2 h before confinement, spent medium was discarded and replaced with fresh medium containing the 6.58-µm polystyrene spacer beads to allow beads to settle. Then, cells underwent the same exact mechanical confinement assay. iPSCs only underwent a single cycle (one ∼8 h confinement).

Journal of Cell Science (2023) 136, jcs260753. doi:10.1242/jcs.260753

Unsynchronized A549 cells underwent four sessions of 8 h confinement for short-term studies or 12 sessions for long-term kinetics studies. These A549 cells were passaged as needed to avoid over-confluency.

MPS1i inhibitor reversine and AZ3146 treatment combined with confinement for flow cytometry (Fig. 2Aii,B) follows the no-synchronization protocol for 4 days (Fig. S3Dii), and drug was washed out when confinement was released. The corresponding dose-testing experiments were conducted with the same timeline, except that confinement was replaced with different doses of MPS1 inhibitory drugs.

Live-imaging of *in vitro* mechanical confinement

For live-imaging of mechanical confinement, A549 cells with monoallelic GFP–H2B cells or iPSCs with Hoescht 33342 staining were used and prepared accordingly as described above. Images were taken while cells underwent confinement every 20 min using Olympus IX71 with a digital camera and a 20×/0.4 NA objective. For all confinement assays, an unconfined 2D control was maintained. The 2D control culture was plated at a quarter of the density used for the confined cultures so that both samples could be passaged simultaneously later on. For analysis of abnormal mitosis from treatment with the MPS1i reversine combined with confinement (Fig. 2Aiii; Fig. S3F,G), the sample was synchronized, and MPS1i was added within the same time span as confinement, or applied together. Measurements were taken at specified time points.

To quantify cell death resulting from confinement, we used A549 cells with the Chr-5 RFP–LMNB1 reporter and a GFP–H2B tag for nuclear localization and viability assessment. Cells were synchronized with nocodazole as previously described above (see Treatments section), and after nocodazole washout, fresh medium with 1 µM DAPI was added. Cells were then incubated at 37°C for ∼5 min for DAPI to diffuse and penetrate. Well plates were marked with dots on bottom prior to assay, and images were taken to define the status of cells prior to confinement. Afterwards, confinement continued normally for ∼8 h as described previously, with images taken at distinct timepoints at the same marked locations. Spent medium was discarded and replaced with fresh medium with 1 µM DAPI again 27 h for a ∼10-min incubation after the assay initially began (and for all subsequent imaging timepoints) for live/dead discrimination. Images were taken again at marked locations. Medium with DAPI was always discarded after imaging and replaced with fresh culture medium.

Quantification of abnormal mitosis during confinement using confocal microscopy

Both A549 cells and iPSCs were plated at the same densities described in the '*In vitro* mechanical confinement assays' section on top of sterile 30-mm glass coverslips. For A549 cells, nocodazole synchronization was done as previously described. Polystyrene spacer beads were also added to cultures as previously described. On the day of assay, 1.5 ml of complete culture medium per well was added to as many wells of an ultra-low attachment 6-well plate (Corning) as needed. The 30-mm glass coverslips with the cells adhered to them were then flipped upside down and transferred to the ultra-low attachment 6-well plate to create a 'sandwich' in which the cells were between plastic and glass layers. A sterile stainless weight was then added to the top of the glass coverslip to begin confinement. After 1–2 h had elapsed, the weight was removed, and the glass coverslip with cells was flipped back to its original position (so cells were no longer sandwiched) and transferred to a clean 6-well plate for fixation using 4% paraformaldehyde. Confocal imaging was performed on a Leica TCS SP8 system with a 63×/1.4 NA oil-immersion.

Image acquisition for measurement of chromatin height during confinement

For unconfined measurements of chromatin, both A549 cells and iPSCs were plated at the same densities described in the '*In vitro* mechanical confinement assays' section on top of sterile 35-mm glass bottom Petri dishes (MaTek, Catalog no. p35G-1.5-14-C). For A549 cells, nocodazole synchronization was undertaken as described above. After nocodazole release, cells were stained with 8 µM Hoechst 33342 for at least 15 min prior to imaging. For measurements under confinement, both A549 cells and iPSCs were plated at the same densities described in the '*In vitro* mechanical confinement assays' section on 30-mm glass coverslips. For A549 cells, nocodazole (Noc) synchronization was again performed as previously described. After nocodazole release, cells were replenished with fresh culture medium with 8 µM Hoechst 33342 for DNA staining. The glass coverslip with cells was then flipped upside down and placed on top of a 40-mm length rectangular glass coverslip with 30 µl droplet of 6.58-µm polystyrene spacer beads in complete media (prepared prior to DNA staining) to complete the confinement sandwich. The sandwich was then placed on microscope, with one or more stainless steel metal weights added on top of the coverslip to initiate confinement (No submerging in media). One or more stainless steel metal weights were then added on top of the top coverslip to initiate confinement. For tumor and teratoma chromatin height measurements, freshly harvested samples were fixed overnight using 4% paraformaldehyde at 4°C, permeabilized using 0.5% (v/v) Triton-X for 1 h at room temperature, and finally stained with Hoescht 33342 overnight at 4°C. Small tumor or teratoma sections were sliced, submerged in 20–40 µl of PBS on a rectangular coverslip (either 35×50 or 45×50 mm^2). All samples were imaged using a Leica TCS SP8 system with a 63×/1.4 NA oil-immersion. All images were taken every 0.5 µm along the focus (*Z*-stack) to cover the entire nuclei, whether it be interphase or mitotic. All image stacks were 3D-reconstructed using ImageJ. The first frame was used as the top view, and the tenth frame was used as the side view in a 36-frame 3D construction profile. For tumor and teratoma sections, the thinnest portion of the nucleus is treated as the height, due to the 3D nature of the sample preventing determination of the nucleus orientation.

Mouse models and xenograft dissociation

For *in vivo* studies, non-obese diabetic/severe combined immunodeficient (NOD/SCID) mice with null expression of interleukin-2 receptor gamma chain (referred to in text as NSG mice) were used (Swift et al., 2013). Mice were procured by the University of Pennsylvania Stem Cell and Xenograft Core. Mouse xenografts were generated in 8- to 12-week-old NSG mice by subcutaneous or intraperitoneal injection (as a 100 µl bolus) of ∼0.5×10^6–1.0×10^6 A549 cancer cells (for tumors) or iPSCs (for teratomas). For injection, cells were resuspended in sterile, serum-free media with Matrigel at a 7:3 volumetric ratio. Tumor area was calculated as $A=\pi/4\times L\times W$, where L and W represent length and width, respectively. For all *in vivo* studies, tumor and teratomas were grown up until they reached ∼2-cm in either length or width, after which mice were humanely euthanized. All mouse experiments were planned with and performed in accordance with protocols approved by the University of Pennsylvania's Institutional Animal Care & Use Committee.

For dissociation, tumor and teratomas from humanely euthanized mice (killed by means of CO_2 inhalation and subsequent confirmatory cervical dislocation) were disaggregated using dispase (Corning, Catalog no. 354235) supplemented with 4 mg ml^{-1} collagenase IV (Thermo FIsher Scientific, Catalog no. 17104-019) and DNase I (Thermo Fisher Scientific, Catalog no. 18068-015) at 1 µl per 1 ml of dispase solution. Tumor and teratomas were allowed to dissociate for 30 min while being incubated at 37°C. Dissociated cells were centrifuged at 300 ***g*** for 10 min, washed with Dulbecco's phosphate-buffered saline (PBS; Gibco, Catalog no. 10010-023), and resuspended in ACK lysis buffer to lyse red blood cells. After lysis, cells were washed once more and used for flow cytometry quantification, single-cell sequencing experiments, or plated back following the cell culture methods described above.

Power-law scaling *in vitro* and *in vivo*

Scaling calculations as depicted in Fig. 3H were performed as follows: for cells in tumors, cell number was calculated based on number/cm^3 estimated from tumor section images using 3D reconstruction (ImageJ) from confocal microscopy and the volume of each tumor recorded prior to dissociation. For *in vitro* cell number calculations, all A549 RFP–LMNB1 clones were cultured for 278 days after being FACS-enriched and were left unperturbed for the entire duration. Cells were only passaged at ∼70–80% confluency

(and at each passaging timepoint, a sample of cells was analyzed via flow cytometry for reporter-negative quantification). The cell number used for analysis is the theoretical total number of cells that would have been generated from the original culture (assuming an infinitely large culture vessel and unlimited nutrients). For scaling calculation associated with MPS1 inhibition and confinement kinetics in Fig. 4G,H,J, cell number is calculated in similar way as for the theoretical total number described above. However, doubling time for each condition is not necessarily the same: for A549 MPS1 inhibition and DMSO control, cells were seeded at low density and did not reach full confluency before passaging, so the normal doubling time of A549 in this study (~19 h) is used; for confinement and its control, however, cells were seeded at a semi-confluent density to start, and cell number was calculated based on the logistic growth function, passaged every 4 days, and assuming all cells dissociated each time were plated back for the next cycle.

Tumor staining

Tumors were excised, fixed in 4% formaldehyde overnight at 4°C, washed in PBS, and dehydrated in 70% ethanol prior to submission. Imaging was undertaken using an Olympus IX inverted microscope with a 40×/0.6 NA or 20×/0.4 NA objective and equipped with a sCMOS camera or a Leica TCS SP8 system with a 63X/1.4 NA oil-immersion (provided and maintained by the University of Pennsylvania Cell & Developmental Biology Microscopy Core).

Quantitation and statistical analysis

Statistical methods were not used to predetermine sample size. The experiments were not randomized. Anonymization to the allocation during experiments and outcome assessment was not undertaken. The statistical methods for each experiment are included in the corresponding figure legends. All statistical analyses were undertaken on GraphPad Prism 9.0. All experiments were biologically repeated and confirmed. Additionally, at least two separate investigators performed each experiment separately, for reproducibility.

Acknowledgements

We acknowledge technical contributions from Dazhen Liu, Jacqueline Hui Zhu. We gratefully acknowledge core facilities at the University of Pennsylvania Perelman School of Medicine for instrument access and assistance: Flow Cytometry and Cell Sorting Core, Stem Cell and Xenograft Core, Molecular Pathology and Imaging Core, Screening Core, and the Cell & Developmental Biology Microscopy Core. We also thank The Center for Applied Genomics Core in The Children's Hospital of Philadelphia for running SNPa experiments.

Competing interests

The authors declare no competing or financial interests.

Author contributions

Conceptualization: D.E.D., C.R.P., Y.X., J.I.; Methodology: D.E.D., C.R.P., Y.X., P.K.Z., M.W., B.H.H., S.P., J.C.A., J.D., M.P.T., A.A., L.J.D., M.L.; Software: M.V., J.I., Y.X., M.W.; Validation: D.E.D.; Formal analysis: D.E.D., C.R.P., Y.X., P.K.Z., M.W., B.H.H., J.C.A.,; Investigation: D.E.D., C.R.P., Y.X., P.K.Z., M.W., B.H.H., J.C.A.,; Resources: D.E.D.; Data curation: D.E.D., C.R.P., Y.X., P.K.Z., M.W., B.H.H.; Writing - original draft: D.E.D., C.R.P., Y.X., P.K.Z., M.W., B.H.H., S.P.; Writing - review & editing: D.E.D.; Supervision: D.E.D.; Project administration: D.E.D.; Funding acquisition: D.E.D., B.H.H., J.C.A., J.I., L.J.D.

Funding

This work was supported by funding from the National Institutes of Health - National Cancer Institute or National Heart, Lung, and Blood Institute (U54 CA193417, U01 CA254886, R01 HL124106, P01 CA265794), grants from the National Science Foundation (MRSEC DMR-1720530 and DMR-1420530 and Grant Agreements CMMI 1548571 and 154857), Human Frontier Science Program Grant RGP00247/2017, and Pennsylvania Department of Health Grant HRFF 4100083101. B.H.H., M.P.T., and J.C.A. are supported by Graduate Research Fellowships from the National Science Foundation (DGE-1845298). The content of this article is solely the responsibility of the authors and does not represent official views of the National Institutes of Health or the National Science Foundation. Deposited in PMC for release after 12 months.

Data availability

All relevant data can be found within the article and its supplementary information.

Peer review history

The peer review history is available online at https://journals.biologists.com/jcs/lookup/doi/10.1242/jcs.260753.reviewer-comments.pdf

References

Alvey, C. M., Spinler, K. R., Irianto, J., Pfeifer, C. R., Hayes, B., Xia, Y., Cho, S., Dingal, P. C. P. D., Hsu, J., Smith, L. et al. (2017). SIRPA-inhibited, marrow-derived macrophages engorge, accumulate, and differentiate in antibody-targeted regression of solid tumors. *Curr. Biol.* **27**, 2065-2077.e6. doi:10.1016/j.cub.2017.06.005

Aran, D., Looney, A. P., Liu, L., Wu, E., Fong, V., Hsu, A., Chak, S., Naikawadi, R. P., Wolters, P. J., Abate, A. R. et al. (2019). Reference-based analysis of lung single-cell sequencing reveals a transitional profibrotic macrophage. *Nat. Immunol.* **20**, 163-172. doi:10.1038/s41590-018-0276-y

Booth, A. J. R., Yue, Z., Eykelenboom, J. K., Stiff, T., Luxton, G. W. G., Hochegger, H. and Tanaka, T. U. (2019). Contractile acto-myosin network on nuclear envelope remnants positions human chromosomes for mitosis. *Elife* **8**, e46902. doi:10.7554/eLife.46902

Brito, D. A. and Rieder, C. L. (2006). Mitotic checkpoint slippage in humans occurs via cyclin B destruction in the presence of an active checkpoint. *Curr. Biol.* **16**, 1194-1200. doi:10.1016/j.cub.2006.04.043

Conti, M. A., Saleh, A. D., Brinster, L. R., Cheng, H., Chen, Z., Cornelius, S., Liu, C., Ma, X., Van Waes, C. and Adelstein, R. S. (2015). Conditional deletion of nonmuscle myosin II-A in mouse tongue epithelium results in squamous cell carcinoma. *Sci. Rep.* **5**, 14068. doi:10.1038/srep14068

Davoli, T., Xu, A. W., Mengwasser, K. E., Sack, L. M., Yoon, J. C., Park, P. J. and Elledge, S. J. (2013). Cumulative haploinsufficiency and triplosensitivity drive aneuploidy patterns and shape the cancer genome. *Cell* **155**, 948-962. doi:10.1016/j.cell.2013.10.011

Dumont, S. and Mitchison, T. J. (2009). Compression regulates mitotic spindle length by a mechanochemical switch at the poles. *Curr. Biol.* **19**, 1086-1095. doi:10.1016/j.cub.2009.05.056

Eggan, K., Rode, A., Jentsch, I., Samuel, C., Hennek, T., Tintrup, H., Zevnik, B., Erwin, J., Loring, J., Jackson-Grusby, L. et al. (2002). Male and female mice derived from the same embryonic stem cell clone by tetraploid embryo complementation. *Nat. Biotechnol.* **20**, 455-459. doi:10.1038/nbt0502-455

Engler, A., Bacakova, L., Newman, C., Hategan, A., Griffin, M. and Discher, D. (2004). Substrate compliance versus ligand density in cell on gel responses. *Biophys. J.* **86**, 617-628. doi:10.1016/S0006-3495(04)74140-5

Engler, A. J., Sen, S., Sweeney, H. L. and Discher, D. E. (2006). Matrix elasticity directs stem cell lineage specification. *Cell* **126**, 677-689. doi:10.1016/j.cell.2006.06.044

Farr, C. J., Antoniou-Kourounioti, M., Mimmack, M. L., Volkov, A. and Porter, A. C. (2014). The alpha isoform of topoisomerase II is required for hypercompaction of mitotic chromosomes in human cells. *Nucleic Acids Res.* **42**, 4414-4426. doi:10.1093/nar/gku076

Hafemeister, C. and Satija, R. (2019). Normalization and variance stabilization of single-cell RNA-seq data using regularized negative binomial regression. *Genome Biol.* **20**, 296. doi:10.1186/s13059-019-1874-1

Han, K., Pierce, S. E., Li, A., Spees, K., Anderson, G. R., Seoane, J. A., Lo, Y. H., Dubreuil, M., Olivas, M., Kamber, R. A. et al. (2020). CRISPR screens in cancer spheroids identify 3D growth-specific vulnerabilities. *Nature* **580**, 136-141. doi:10.1038/s41586-020-2099-x

Hiruma, Y., Sacristan, C., Pachis, S. T., Adamopoulos, A., Kuijt, T., Ubbink, M., Von Castelmur, E., Perrakis, A. and Kops, G. J. (2015). CELL DIVISION CYCLE. Competition between MPS1 and microtubules at kinetochores regulates spindle checkpoint signaling. *Science* **348**, 1264-1267. doi:10.1126/science.aaa4055

Hiruma, Y., Koch, A., Dharadhar, S., Joosten, R. P. and Perrakis, A. (2016). Structural basis of reversine selectivity in inhibiting Mps1 more potently than aurora B kinase. *Proteins* **84**, 1761-1766. doi:10.1002/prot.25174

Huang, H. C., Mitchison, T. J. and Shi, J. (2010). Stochastic competition between mechanistically independent slippage and death pathways determines cell fate during mitotic arrest. *PLoS One* **5**, e15724. doi:10.1371/journal.pone.0015724

Joo, E. E. and Yamada, K. M. (2014). MYPT1 regulates contractility and microtubule acetylation to modulate integrin adhesions and matrix assembly. *Nat. Commun.* **5**, 3510. doi:10.1038/ncomms4510

Knouse, K. A., Lopez, K. E., Bachofner, M. and Amon, A. (2018). Chromosome segregation fidelity in epithelia requires tissue architecture. *Cell* **175**, 200-211.e13. doi:10.1016/j.cell.2018.07.042

Lancaster, O. M., Le Berre, M., Dimitracopoulos, A., Bonazzi, D., Zlotek-Zlotkiewicz, E., Picone, R., Duke, T., Piel, M. and Baum, B. (2013). Mitotic rounding alters cell geometry to ensure efficient bipolar spindle formation. *Dev. Cell* **25**, 270-283. doi:10.1016/j.devcel.2013.03.014

Ma, X., Jana, S. S., Conti, M. A., Kawamoto, S., Claycomb, W. C. and Adelstein, R. S. (2010). Ablation of nonmuscle myosin II-B and II-C reveals a role for nonmuscle myosin II in cardiac myocyte karyokinesis. *Mol. Biol. Cell* **21**, 3952-3962. doi:10.1091/mbc.e10-04-0293

Mabbott, N. A., Baillie, J. K., Brown, H., Freeman, T. C. and Hume, D. A. (2013). An expression atlas of human primary cells: inference of gene function from coexpression networks. *BMC Genomics* **14**, 632. doi:10.1186/1471-2164-14-632

Mandai, M., Watanabe, A., Kurimoto, Y., Hirami, Y., Morinaga, C., Daimon, T., Fujihara, M., Akimaru, H., Sakai, N., Shibata, Y. et al. (2017). Autologous induced stem-cell-derived retinal cells for macular degeneration. *N. Engl. J. Med.* **376**, 1038-1046. doi:10.1056/NEJMoa1608368

Matthews, H. K., Ganguli, S., Plak, K., Taubenberger, A. V., Win, Z., Williamson, M., Piel, M., Guck, J. and Baum, B. (2020). Oncogenic signaling alters cell shape and mechanics to facilitate cell division under confinement. *Dev. Cell* **52**, 563-573.e3. doi:10.1016/j.devcel.2020.01.004

Meng, Z., Qiu, Y., Lin, K. C., Kumar, A., Placone, J. K., Fang, C., Wang, K. C., Lu, S., Pan, M., Hong, A. W. et al. (2018). RAP2 mediates mechanoresponses of the Hippo pathway. *Nature* **560**, 655-660. doi:10.1038/s41586-018-0444-0

Nava, M. M., Miroshnikova, Y. A., Biggs, L. C., Whitefield, D. B., Metge, F., Boucas, J., Vihinen, H., Jokitalo, E., Li, X., Garcia Arcos, J. M. et al. (2020). Heterochromatin-driven nuclear softening protects the genome against mechanical stress-induced damage. *Cell* **181**, 800-817.e22. doi:10.1016/j.cell.2020.03.052

Nielsen, C. F., Zhang, T., Barisic, M., Kalitsis, P. and Hudson, D. F. (2020). Topoisomerase IIalpha is essential for maintenance of mitotic chromosome structure. *Proc. Natl. Acad. Sci. USA* **117**, 12131-12142. doi:10.1073/pnas.2001760117

Parajon, E., Surcel, A. and Robinson, D. N. (2021). The mechanobiome: a goldmine for cancer therapeutics. *Am. J. Physiol. Cell Physiol.* **320**, C306-C323. doi:10.1152/ajpcell.00409.2020

Paszek, M. J., Dufort, C. C., Rossier, O., Bainer, R., Mouw, J. K., Godula, K., Hudak, J. E., Lakins, J. N., Wijekoon, A. C., Cassereau, L. et al. (2014). The cancer glycocalyx mechanically primes integrin-mediated growth and survival. *Nature* **511**, 319-325. doi:10.1038/nature13535

Petridou, N. I., Corominas-Murtra, B., Heisenberg, C. P. and Hannezo, E. (2021). Rigidity percolation uncovers a structural basis for embryonic tissue phase transitions. *Cell* **184**, 1914-1928.e19. doi:10.1016/j.cell.2021.02.017

Pfeifer, C. R., Alvey, C. M., Irianto, J. and Discher, D. E. (2017). Genome variation across cancers scales with tissue stiffness - an invasion-mutation mechanism and implications for immune cell infiltration. *Curr. Opin. Syst. Biol.* **2**, 103-114. doi:10.1016/j.coisb.2017.04.005

Pfeifer, C. R., Xia, Y., Zhu, K., Liu, D., Irianto, J., Garcia, V. M. M., Millan, L. M. S., Niese, B., Harding, S., Deviri, D. et al. (2018). Constricted migration increases DNA damage and independently represses cell cycle. *Mol. Biol. Cell* **29**, 1948-1962. doi:10.1091/mbc.E18-02-0079

Picariello, H. S., Kenchappa, R. S., Rai, V., Crish, J. F., Dovas, A., Pogoda, K., Mcmahon, M., Bell, E. S., Chandrasekharan, U., Luu, A. et al. (2019). Myosin IIA suppresses glioblastoma development in a mechanically sensitive manner. *Proc. Natl. Acad. Sci. USA* **116**, 15550-15559. doi:10.1073/pnas.1902847116

Przybyla, L., Muncie, J. M. and Weaver, V. M. (2016). Mechanical control of epithelial-to-mesenchymal transitions in development and cancer. *Annu. Rev. Cell Dev. Biol.* **32**, 527-554. doi:10.1146/annurev-cellbio-111315-125150

Raab, M., Swift, J., Dingal, P. C., Shah, P., Shin, J. W. and Discher, D. E. (2012). Crawling from soft to stiff matrix polarizes the cytoskeleton and phosphoregulates myosin-II heavy chain. *J. Cell Biol.* **199**, 669-683. doi:10.1083/jcb.201205056

Rancati, G., Pavelka, N., Fleharty, B., Noll, A., Trimble, R., Walton, K., Perera, A., Staehling-Hampton, K., Seidel, C. W. and Li, R. (2008). Aneuploidy underlies rapid adaptive evolution of yeast cells deprived of a conserved cytokinesis motor. *Cell* **135**, 879-893. doi:10.1016/j.cell.2008.09.039

Roberts, B., Haupt, A., Tucker, A., Grancharova, T., Arakaki, J., Fuqua, M. A., Nelson, A., Hookway, C., Ludmann, S. A., Mueller, I. A. et al. (2017). Systematic gene tagging using CRISPR/Cas9 in human stem cells to illuminate cell organization. *Mol. Biol. Cell* **28**, 2854-2874. doi:10.1091/mbc.e17-03-0209

Rosenblatt, J., Cramer, L. P., Baum, B. and Mcgee, K. M. (2004). Myosin II-dependent cortical movement is required for centrosome separation and positioning during mitotic spindle assembly. *Cell* **117**, 361-372. doi:10.1016/S0092-8674(04)00341-1

Samejima, K., Samejima, I., Vagnarelli, P., Ogawa, H., Vargiu, G., Kelly, D. A., De Lima Alves, F., Kerr, A., Green, L. C., Hudson, D. F. et al. (2012). Mitotic chromosomes are compacted laterally by KIF4 and condensin and axially by topoisomerase IIalpha. *J. Cell Biol.* **199**, 755-770. doi:10.1083/jcb.201202155

Santaguida, S., Tighe, A., D'Alise, A. M., Taylor, S. S. and Musacchio, A. (2010). Dissecting the role of MPS1 in chromosome biorientation and the spindle checkpoint through the small molecule inhibitor reversine. *J. Cell Biol.* **190**, 73-87. doi:10.1083/jcb.201001036

Schramek, D., Sendoel, A., Segal, J. P., Beronja, S., Heller, E., Oristian, D., Reva, B. and Fuchs, E. (2014). Direct in vivo RNAi screen unveils myosin IIa as a tumor suppressor of squamous cell carcinomas. *Science* **343**, 309-313. doi:10.1126/science.1248627

Sedzinski, J., Biro, M., Oswald, A., Tinevez, J. Y., Salbreux, G. and Paluch, E. (2011). Polar actomyosin contractility destabilizes the position of the cytokinetic furrow. *Nature* **476**, 462-466. doi:10.1038/nature10286

Segel, M., Neumann, B., Hill, M. F. E., Weber, I. P., Viscomi, C., Zhao, C., Young, A., Agley, C. C., Thompson, A. J., Gonzalez, G. A. et al. (2019). Niche stiffness underlies the ageing of central nervous system progenitor cells. *Nature* **573**, 130-134. doi:10.1038/s41586-019-1484-9

Shaffer, S. M., Dunagin, M. C., Torborg, S. R., Torre, E. A., Emert, B., Krepler, C., Beqiri, M., Sproesser, K., Brafford, P. A., Xiao, M. et al. (2017). Rare cell variability and drug-induced reprogramming as a mode of cancer drug resistance. *Nature* **546**, 431-435. doi:10.1038/nature22794

Skamagki, M., Correia, C., Yeung, P., Baslan, T., Beck, S., Zhang, C., Ross, C. A., Dang, L., Liu, Z., Giunta, S. et al. (2017). ZSCAN10 expression corrects the genomic instability of iPSCs from aged donors. *Nat. Cell Biol.* **19**, 1037-1048. doi:10.1038/ncb3598

Skowyra, A., Allan, L. A., Saurin, A. T. and Clarke, P. R. (2018). USP9X limits mitotic checkpoint complex turnover to strengthen the spindle assembly checkpoint and guard against chromosomal instability. *Cell Rep.* **23**, 852-865. doi:10.1016/j.celrep.2018.03.100

Stewart, M. P., Helenius, J., Toyoda, Y., Ramanathan, S. P., Muller, D. J. and Hyman, A. A. (2011). Hydrostatic pressure and the actomyosin cortex drive mitotic cell rounding. *Nature* **469**, 226-230. doi:10.1038/nature09642

Straight, A. F., Cheung, A., Limouze, J., Chen, I., Westwood, N. J., Sellers, J. R. and Mitchison, T. J. (2003). Dissecting temporal and spatial control of cytokinesis with a myosin II inhibitor. *Science* **299**, 1743-1747. doi:10.1126/science.1081412

Stuart, T., Butler, A., Hoffman, P., Hafemeister, C., Papalexi, E., Mauck, W. M., 3rd, Hao, Y., Stoeckius, M., Smibert, P. and Satija, R. (2019). Comprehensive integration of single-cell data. *Cell* **177**, 1888-1902.e21. doi:10.1016/j.cell.2019.05.031

Sudo, H. (2018). Microtubule hyperacetylation enhances KL1-dependent micronucleation under a Tau deficiency in mammary epithelial cells. *Int. J. Mol. Sci.* **19**, 2488. doi:10.3390/ijms19092488

Swift, J., Ivanovska, I. L., Buxboim, A., Harada, T., Dingal, P. C., Pinter, J., Pajerowski, J. D., Spinler, K. R., Shin, J. W., Tewari, M. et al. (2013). Nuclear lamin-A scales with tissue stiffness and enhances matrix-directed differentiation. *Science* **341**, 1240104. doi:10.1126/science.1240104

Taneja, N., Bersi, M. R., Baillargeon, S. M., Fenix, A. M., Cooper, J. A., Ohi, R., Gama, V., Merryman, W. D. and Burnette, D. T. (2020). Precise tuning of cortical contractility regulates cell shape during cytokinesis. *Cell Rep.* **31**, 107477. doi:10.1016/j.celrep.2020.03.041

Thompson, S. L. and Compton, D. A. (2008). Examining the link between chromosomal instability and aneuploidy in human cells. *J. Cell Biol.* **180**, 665-672. doi:10.1083/jcb.200712029

Tickle, T., Tirosh, I., Georgescu, C., Brown, M. and Haas, B. (2019). *inferCNV of the Trinity CTAT Project*. Cambridge, MA, USA: Klarman Cell Observatory, Broad Institute of MIT and Harvard.

Tomasetti, C. and Vogelstein, B. (2015). Cancer etiology. Variation in cancer risk among tissues can be explained by the number of stem cell divisions. *Science* **347**, 78-81. doi:10.1126/science.1260825

Uhler, C. and Shivashankar, G. V. (2017). Regulation of genome organization and gene expression by nuclear mechanotransduction. *Nat. Rev. Mol. Cell Biol.* **18**, 717-727. doi:10.1038/nrm.2017.101

Umbreit, N. T., Zhang, C. Z., Lynch, L. D., Blaine, L. J., Cheng, A. M., Tourdot, R., Sun, L., Almubarak, H. F., Judge, K., Mitchell, T. J. et al. (2020). Mechanisms generating cancer genome complexity from a single cell division error. *Science* **368**, eaba0712. doi:10.1126/science.aba0712

Vitiello, E., Moreau, P., Nunes, V., Mettouchi, A., Maiato, H., Ferreira, J. G., Wang, I. and Balland, M. (2019). Acto-myosin force organization modulates centriole separation and PLK4 recruitment to ensure centriole fidelity. *Nat. Commun.* **10**, 52. doi:10.1038/s41467-018-07965-6

Xia, Y., Pfeifer, C. R., Zhu, K., Irianto, J., Liu, D., Pannell, K., Chen, E. J., Dooling, L. J., Tobin, M. P., Wang, M. et al. (2019). Rescue of DNA damage after constricted migration reveals a mechano-regulated threshold for cell cycle. *J. Cell Biol.* **218**, 2545-2563. doi:10.1083/jcb.201811100

Yizhak, K., Aguet, F., Kim, J., Hess, J. M., Kubler, K., Grimsby, J., Frazer, R., Zhang, H., Haradhvala, N. J., Rosebrock, D. et al. (2019). RNA sequence analysis reveals macroscopic somatic clonal expansion across normal tissues. *Science* **364**, eaaw0726. doi:10.1126/science.aaw0726